La Rivista del Nuovo Cimento
https://doi.org/10.1007/s40766-024-00062-z

Spin–orbit coupling in quantum materials: emergent phenomena, their modelling and examples from two-dimensional magnets

Silvia Picozzi[1,2]

Received: 28 May 2024 / Accepted: 29 October 2024

Abstract
Acknowledging spin–orbit coupling (SOC) as a pivotal microscopic ingredient in quantum materials, this paper provides a comprehensive overview of spin–orbit-driven phenomena and effects in magnetic, non-magnetic and multiferroic materials. As for magnets, the review discusses SOC-induced magnetic anisotropy, exotic spin–spin interactions, and their implications on the emergence of complex spin textures. It also explores band-splitting effects in non-magnetic solids, with a focus on Rashba effects and spin-valley coupling. Additionally, the emergence of ferroelectric polarization from non-collinear spin textures in multiferroics is examined. The paper analyzes methods for estimating SOC-related quantities from first principles within the density functional theory, particularly exchange coupling tensors and magnetoelectric coupling tensors. Finally, it presents case studies on two-dimensional magnetic materials, including the characterization of peculiar Kitaev-like exchange coupling and the investigation of multiferroicity in NiI_2 monolayers. Overall, the paper delves into the microscopic mechanisms related to SOC, by offering insights into the diverse effects and manifestations of SOC in the quantum materials world.

Keywords Spin–orbit coupling · Magnetism · Spin · Density functional theory

1 Introduction

Since its dawn, research in solid-state magnetism has traditionally focused on the elemental solids constituted by the first row of transition metals (*i.e.* with partially filled 3*d* shell, particularly on iron, cobalt, and nickel) and their alloys. These materials are renowned for their ferromagnetic properties and characterized mostly by itinerant magnetism [1]. The wealth of technological applications that this research

✉ Silvia Picozzi
silvia.picozzi@unimib.it

1 Dipartimento di Scienza dei Materiali, Universitá degli Studi di Milano-Bicocca, Via Roberto Cozzi 55, 20125 Milan, Italy

2 Consiglio Nazionale delle Ricerche, CNR-SPIN, c/o Universitá "G. D'Annunzio", 66100 Chieti, Italy

Published online: 07 April 2025

led to, undoubtedly made magnetism one of the areas of condensed matter physics, where ideas and discoveries most quickly turned into groundbreaking technologies [2, 3]. Indeed, in nowadays information technology, very often the spin of the electron is used for storage and manipulation of data. In the last couple of decades of the twentieth century, attention has partially shifted and has also been largely devoted to systems characterized by localized spins, mainly correlated insulators (or at most "weak" metals), such as $3d$ transition metal oxides, with their fascinating and rich physics, various mechanisms for magnetic orders (such as superexchange, double exchange, etc.), coupled to other phenomena, such as Jahn-Teller interactions, intertwined charge/orbital/spin orders, unusual magneto-transport, etc. During the first 2 decades of the twenty first century, the focus of research in solid-state magnetism has increasingly turned towards the intriguing and much less explored realm of "spin–orbit-related magnetism". Materials containing heavy ions with partially-filled d and f electronic shells exhibit a variety of unconventional quantum states, including skyrmions and other topological phases, exotic band-splitting phenomena, and possibly multipolar orders, quantum spin liquids, etc. The significant spin–orbit interaction arising from the heavy nuclei of both magnetic ions and non–magnetic ligands affects the coupling of corresponding on-site moments and leads to the emergence of spin–orbital-entangled ground states, sometimes challenging our traditional understanding of spin and orbital degrees of freedom [4, 5]. Moreover, the interaction of the latter with lattice degrees of freedom, applied fields and other external perturbations (strain, pressure, heat, etc) has sparked intense research activity in SOC-related magnetism.

While the field is in continuous evolution and SOC is crucial for an incredibly large number of effects and phenomena in condensed matter physics (superconductivity, Mott-transitions, etc), in this Review, we will concentrate on some selected aspects of the rich physics and emergent phenomena that SOC gives rise to. While the modelling of this complex field is not straightforward and several different approaches exist to tackle SOC-related phenomena, we will focus on density functional theory as an efficient theoretical tool and discuss how to estimate from first-principles the relevant properties of interest for a realistic modelling of SOC-related effects. In the final part, we will show some specific examples and results of SOC-induced phenomena related to ferroic materials, with special emphasis on 2D magnets.

2 Spin–orbit coupling in solids

2.1 From atoms to solids

Before moving to solids, let us start by SOC in atoms. The spin–orbit interaction, along with the spin as an attribute of the electron, naturally emerges from the Dirac equation, within a relativistic single particle theory [6]. The so-called Pauli equation (an approximate expression of the Dirac equation for the large component only of the wave-function) can be expressed as:

$$[E + eV(r) - \frac{1}{2m}(\mathbf{p}(\mathbf{r}) + \frac{e}{c}\mathbf{A}(\mathbf{r}))^2 + \frac{1}{2mc^2}(E + eV(r))^2$$

$$+i\frac{e\hbar}{(2mc)^2}\mathbf{E}(\mathbf{r})\cdot\mathbf{p}-\frac{e\hbar}{(2mc)^2}\sigma\cdot(\mathbf{E}(\mathbf{r})\times\mathbf{p})-\frac{e\hbar}{2mc}\sigma\cdot\mathbf{B}(\mathbf{r})]\psi=0 \quad (1)$$

where $V(\mathbf{r})$ and $\mathbf{A}(\mathbf{r})$ represent the scalar and vector potential, respectively, σ is the vector of the Pauli spin matrices, whereas $\mathbf{E}(\mathbf{r})$ and $\mathbf{B}(\mathbf{r})$ denote electric and magnetic fields, respectively. In the non-relativistic limit, the first three terms give rise to the ordinary Schroedinger equation. The fourth term is generally labelled as "mass-velocity" term, as it describes the relativistic correction due to the change of mass with velocity, whereas the $\mathbf{E}(\mathbf{r})\cdot\mathbf{p}$ is denoted as "Darwin" term, having no classical analogue. The last two terms are related to the interaction of the electron spin with magnetic fields, the latter being described as a Zeeman energy, $\mu_B\sigma\cdot\mathbf{B}$ (having introduced the Bohr magneton, $\mu_B=\frac{e\hbar}{2mc}$). The second-last term—from which the spin–orbit coupling originates—will be discussed at length in what follows.

Let us start with a cartoon: in Fig. 1a (see the upper central ellipse, highlighted in red), a scheme of an electron moving close to the nucleus in an electric field $\mathbf{E}$ (*i.e.* a potential gradient) is reported. The electric field is seen by the electron—via a Lorentz transformation—as a magnetic field $\mathbf{B}$, which the electron spin couples to in the form similar to a Zeeman-like interaction. As such, this term describes the interaction between an electron spin and the magnetic field seen by the electron in its local frame as arising from its own motion in an electric field. The relativistic term describes the coupling between σ and the electron orbital motion and is, therefore, called the spin–orbit coupling. We note that the heuristic argument of a Zeeman-like field actually leads to a spin–orbit interaction which is wrong by a factor of two with respect to its value within special relativity, the factor $\frac{1}{2}$ usually referred to as Thomas factor [7, 8]. The expression of relativistic SOC in terms of the interaction between the spin and the orbital moment becomes clearer by the following argument. When moving close to the atomic nucleus, one can assume a spherically symmetric potential $V(r)$ and, going back to Eq. 1, the SOC can be written as proportional to:

$$\sigma\cdot(\mathbf{E}(\mathbf{r})\times\mathbf{p})=\sigma\cdot(\nabla(\mathbf{r})\times\mathbf{p})=\frac{1}{r}\frac{\mathrm{d}V(r)}{\mathrm{d}r}\sigma\cdot(\nabla V(r)\times p)=\frac{1}{r}\frac{\mathrm{d}V(r)}{\mathrm{d}r}\sigma\cdot\mathbf{l}=\xi\,\sigma\cdot\mathbf{l} \quad (2)$$

where $\mathbf{p}$ labels the momentum, $\mathbf{l}$ the orbital moment and ξ is generally referred to as the SOC constant. Here, we have implicitly assumed the Russell-Sanders or LS-coupling scheme to be valid [9]. However, in the case of stronger SOC, the spin and orbital momenta will first couple to form the angular momentum $\mathbf{j}$, so that the jj-coupling scheme is likely to be more adequate. In this review, we will mostly discuss systems based on $3d$ "light" magnetic ions, where the Russell-Saunders scheme is expected to be valid; however, for $5d$ or rare-earth elements, the reader should be aware of possible breaking of the assumptions made so far.

It should be further noted about Eq. 1 that the Pauli spin-matrices $\boldsymbol{\sigma}$ couple the spin-up and spin-down parts of the large wave-function component. Consequently, in the absence of a vector potential, the absence of the $\boldsymbol{\sigma}$ term in both the mass-velocity and Darwin terms warrants their classification as "scalar-relativistic" corrections, indicating a lack of coupling between spin-components of the wave-function.

When moving to crystals, this picture can be still considered as valid. In particular, since the potential radial derivative in a crystal will be maximum close to the nucleus, the largest contribution to SOC will emerge from this region. In addition, close to the nucleus the potential will be Coulomb-like $V(r) \sim -\frac{Z}{r}$, its derivative being also proportional to the atomic number Z. One therefore expects SOC-driven effects to be large (small) for crystals containing heavy (light) atoms. We further stress that SOC links the real-space and the spin-space; in other words, when neglecting SOC, the coordinate system where the spins move is completely decoupled from the lattice/atomic coordinate space.

A note about orbital moment is useful in this context: Within a high-symmetry bulk crystal, such as face-centered cubic (fcc) or body-centered cubic (bcc) structures, the majority of valence electron orbitals are directed toward nearest or next-nearest neighbors. As such, the electron motion is confined to directional bonds, thereby reducing orbital mobility (the so-called “quenching" of orbital moment). Spin–orbit coupling acts against this confinement, and in certain anisotropic crystals and for specific electronic filling of different orbitals, SOC may induce significant orbital moments, counteracting the otherwise suppressed orbital motion imposed by the crystal structure (see for example Ref. [10] for a recent review on orbital physics).

When compared to other energy scales at play in the electronic structure of solids (*i.e.* hybridization, Coulomb repulsion, crystal field effects, etc.), the SOC term is usually much smaller, at least in materials of technological interest, composed by atoms with atomic number $Z <\sim 50$ (*i.e.* leaving aside very heavy atoms, such as actinides). However, despite being a “small" interaction, SOC gives rise to an outstandingly rich variety of physical phenomena, as pictorially shown in Fig. 1. In this review, we will discuss the different effects - and how to model them—in three classes of materials: magnetic materials (Sect. 2.2), non-magnetic materials (Sect. 2.3), multiferroic materials (Sect. 2.4).

In this context, it is worth mentioning that, from an applied perspective, SOC has led to the emergence of “spin–orbitronics," a branch of spintronics (*i.e.* electronics based on the electron spin) that exploits the manipulation of non-equilibrium material properties using SOC. Spin–orbitronics constitutes a very active branch nowadays, aiming at developing low-power spin-based devices, and we refer the reader interested in spin–orbitronics to other reviews [11, 12]. Here, we note that exciting spin-transport and/or spin-to-charge conversion phenomena (such as Spin-Hall effect, [13, 14], spin–orbit torque, [15, 16] Rashba–Edelstein effect, [17] etc) are not going to be covered in this review, which is rather focused on *equilibrium* (*i.e. static*) properties.

2.2 Spin–orbit coupling in magnetic materials

The main effects driven by SOC in magnetic solids are listed below. Let us note that in this review, the focus will mostly be on insulators (or semiconductors), characterized by localized classical spins, *i.e.* each atomic site i is distinguished by a relatively robust magnetic moment $\mathbf{S}_i$ given by a vector quantity, dominantly interacting with other spins in a pairwise fashion, through bonds and/or ligands.

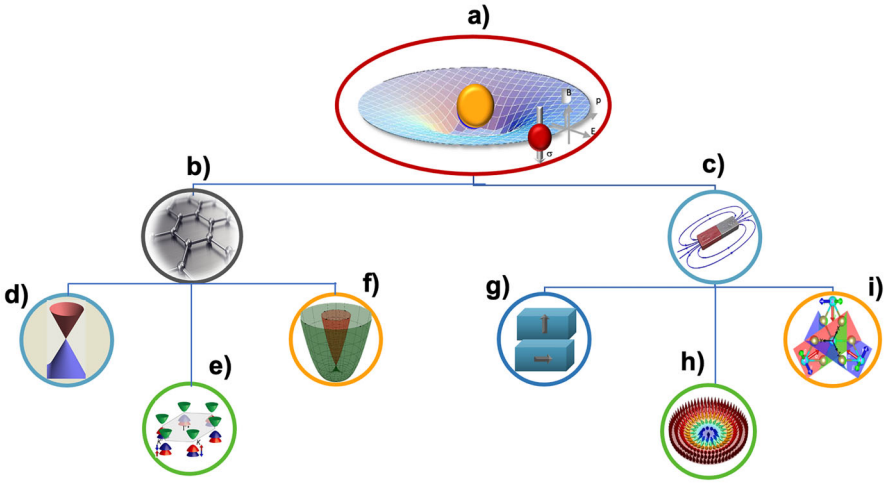

Fig. 1 Pictorial illustration of spin–orbit coupling in both magnetic and non-magnetic solids. **a** SOC in an atomic-like central potential: the yellow sphere represents the nucleus, the red sphere represents the electron in an orbit, with the spin represented by the grey arrow. **b** Main effects of SOC in non-magnetic solids. SOC is at the basis of **d** non-trivial topology (as prototypically represented by a Dirac cone), **e** spin-valley coupling, **f** Rashba–Dresselhaus effects. **c** Main effects of SOC in magnetic solids. SOC is at the basis of **g** magnetic anisotropy (as pictorially represented by ferromagnets having in-plane or out-of-plane magnetization), **h** DM interactions, giving rise to skyrmions, **j** symmetric anisotropic exchange

2.2.1 Magnetic anisotropy

In a long-range magnetically ordered material below the Curie temperature, magnetic anisotropy refers to the energy difference between spins oriented along different directions (taking as reference the crystal axes); as a consequence, each material shows a preferred direction of its spins either along an easy axis or lying in an easy-plane.

Magnetic anisotropy arises due to different microscopic mechanisms, among which the main contributors are: the single ion anisotropy (SIA), the two-ion anisotropy (whose discussion is deferred to the following paragraph) and the dipole–dipole interaction.

The SIA is a form of uniform magneto-crystalline anisotropy, arising from the coupling between the spin and the lattice via relativistic SOC:

$$H_1^{SIA} = \xi \mathbf{L_1} \cdot \mathbf{S_1} = \mathbf{S_1} \cdot \mathbf{A_{11}} \cdot \mathbf{S_1} \tag{3}$$

This equation suggests that, besides the standard coupling between orbital and spin moments, one can express SIA via a tensor (see rightside equality), taking into account all the possible orientations of the $\mathbf{S}_1$ spin in space. The detailed form of the $\mathbf{A}_{11}$ matrix in insulators/semiconductors depends on the symmetry properties, in particular dictated by the arrangement of ligand ions around the magnetic site. In particular, for highly symmetric (*i.e.* cubic) lattice environments of $3d$-based systems, the SIA term ranges in a very small energy scale (*i.e.* μeV), whereas it can increase to

the meV scale for low-symmetry environments and in cases with unquenched orbital moment.

The dipole–dipole interaction is another source of anisotropy, which is often neglected though it can become important in finite-size nanoscale systems, where it is generally dubbed as “shape–anisotropy". While both the dipole–dipole interaction and the SIA can be derived from the relativistic Breit equation (an approximation of Dirac equation), for the dipole–dipole interaction E_d the quantum-mechanical expression is seldom used [18]. Rather, for a crystal with lattice vectors $\mathbf{R}$ and atoms i characterized by localized magnetic moments $\mathbf{S}_i$ at positions τ_i (located in the unit cell), E_d is very often approximated via a classical expression:

$$E_d = \frac{\mu_B^2}{2} \sum_{\mathbf{R},i,j} \frac{\mathbf{S}_i \cdot \mathbf{S}_j}{|\mathbf{R} + \tau_\mathbf{i} - \tau_\mathbf{j}|^3} - 3\frac{[(\mathbf{R} + \tau_\mathbf{i} - \tau_\mathbf{j}) \cdot \mathbf{S}_i][(\mathbf{R} + \tau_\mathbf{i} - \tau_\mathbf{j}) \cdot \mathbf{S}_j]}{|\mathbf{R} + \tau_\mathbf{i} - \tau_\mathbf{j}|^5} \quad (4)$$

We remark that many applications of magnetism are based on magnetic anisotropy, constituting ground for hard-disk-drive technology and related multi-billion market. Although the energy involved to rotate a single spin due to magnetic anisotropy is in general a small quantity (especially for $3d$ bulk metallic materials), the energy required to simultaneously rotate all the spins—strongly coupled by exchange interactions—in a macroscopic magnetic sample will be rather large. Correspondingly, one can evaluate the magnetic field needed to rotate the spins from easy to hard axis, which is of the order of a fraction of a Tesla in iron samples and can increase to a few Tesla for $4f$-based systems.

2.2.2 Spin-canting and exotic interactions among spins

When modelling the exchange interactions with a (pair-wise) spin-Hamiltonian, the main interaction between two spins is the well-known Heisenberg coupling, where two spins are coupled via a scalar term. However, perturbations often occur on top of the Heisenberg-like description.

Following the notation in Ref. Gatteschi et al. [19], by expressing in the most general way a pair-wise exchange interaction, the bilinear spin–spin Hamiltonian can be written as:

$$H_{12} = \mathbf{S_1} \cdot \mathbf{J_{12}} \cdot \mathbf{S_2} = J_{12}\, \mathbf{S_1} \cdot \mathbf{S_2} + \mathbf{S_1} \cdot \mathbf{K_{12}} \cdot \mathbf{S_2} + \mathbf{d_{12}} \cdot (\mathbf{S_1} \times \mathbf{S_2}) \quad (5)$$

where $\mathbf{S}_1$ and $\mathbf{S}_2$ are spin operators for atom 1 and 2, respectively, $\mathbf{J}_{12}$ denotes a 3×3 matrix describing the interaction (see first equality). The second equality stems from the fact that it is always possible to rewrite a matrix-like interaction in an equivalent way, breaking it into three terms: scalar, tensor and vector product of two vector operators (see second equality). The effects of the different terms of Eq. 5 are pictorially illustrated in Fig. 2, as discussed below.

Denoting α, β, γ the Cartesian coordinates, one obtains, for the scalar, tensor and vector contributions:

$$
\begin{aligned}
J_{12} &= \frac{1}{3}\, Tr(\mathbf{J_{12}}) \\
K_{12}^{\alpha\beta} &= \frac{1}{2}(J_{12}^{\alpha\beta} + J_{12}^{\beta\alpha}) - \delta_{\alpha\beta}\frac{1}{3}\, Tr(\mathbf{J_{12}}) \\
d_{12}^{\alpha} &= \frac{1}{2}(J_{12}^{\beta\gamma} - J_{12}^{\gamma\beta}),\ d_{12}^{\beta} = \frac{1}{2}(J_{12}^{\gamma\alpha} - J_{12}^{\alpha\gamma}),\ d_{12}^{\gamma} = \frac{1}{2}(J_{12}^{\alpha\beta} - J_{12}^{\beta\alpha})
\end{aligned}
$$

The scalar term represents the Heisenberg-like contribution, which is invariant under rotations in spin space: it is isotropic, *i.e.* it does not depend on the direction of spins, but only on their relative orientation. The Heisenberg contribution favors either parallel or antiparallel spins, depending on the sign of J_{12}. With the convention defined in Eq. 5, a negative J_{12} defines a ferromagnetic (FM) coupling, while a positive J_{12} defines an antiferromagnetic (AFM) coupling.

The vector part is related to the antisymmetric Dzyaloshinskii–Moriya (DM) interaction ($\mathbf{d}_{12}$ denoting the DM vector), aiming at orienting the two spins perpendicularly and, in general, promoting non-collinearity. Depending on the direction of $\mathbf{d}_{12}$, the DM term tends to cant the spins in a well-defined clockwise or counterclockwise sense; for this reason, it is generally described as a "chiral" interaction. It was originally proposed by Dzyaloshinsky [20] to explain the spin-canting in α-Fe_2O_3, *i.e.* the deviation of the spins from a collinear AFM ordering, so as to give a small net magnetization in the direction perpendicular to the main AFM order parameter. Later on, Moriya contributed to the microscopic understanding of what is now known as Dzyaloshinskii-Moriya interaction (see below) [21].

The tensor term $\mathbf{K}_{12}$ (sometimes referred to as related to the Kitaev exchange [22]) represents the symmetric anisotropic exchange contribution, which favors the spins to be oriented along a specific direction (this is why this term is sometimes referred to as "two-site anisotropy").

Equivalently, upon defining $\mathbf{I}$ as a 3×3 identity matrix, a DM matrix as $\mathbf{D}_{12} = \frac{1}{2}(\mathbf{J_{12}} - \mathbf{J_{12}^T})$ and a Kitaev–like matrix as $\mathbf{K}_{12} = \frac{1}{2}(\mathbf{J_{12}} + \mathbf{J_{12}^T}) - J_{12}\mathbf{I}$, where the superscript T denotes the transpose, one can express: $\mathbf{J_{12}} = J_{12}\mathbf{I} + \mathbf{D_{12}} + \mathbf{K_{12}}$. The antisymmetric DM matrix has only three independent components, which are the components of the DM vector defined above: $d_{12}^x = D_{12}^{yz}$, $d_{12}^y = D_{12}^{zx}$ and $d_{12}^z = D_{12}^{xy}$.

For solid systems, one can trivially extend the atomistic two-site spin-Hamiltonian of Eq. 5 by summing over all the lattice sites (upon taking due care of avoiding double-counting of spin-spin interactions). We also remark that an equivalent expression of the different terms can be formulated in a continuum model or micromagnetic model [23] (*i.e.* an approach through which magnetic materials are treated as having a continuous distribution of magnetic moments—a magnetization $\mathbf{M}(\mathbf{r})$—allowing for a macroscopic description of the properties without considering individual atomic spins or interactions).

We stress that:

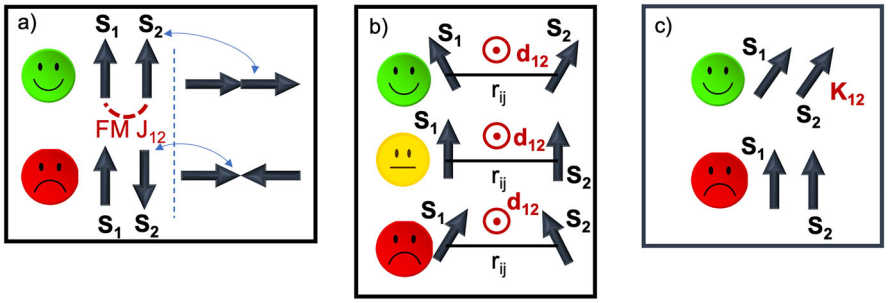

Fig. 2 Effects of different terms in the spin-Hamiltonian to minimize the energy. **a** Heisenberg term: in case of FM exchange coupling, the spins will tend to align parallel rather than antiparallel (obviously, the opposite is true for an opposite sign of the exchange coupling). On the right side (right of the vertical dashed blue separation line), we show the Heisenberg energy term being invariant upon a rotation of the spin pair, represented by blue-curved arrows (in other words, the Heisenberg term is isotropic). **b** DM interaction: the spins tend to cant, so as to optimize the energy deriving from the scalar product between the DM vector and the vector product of the two spins. Obviously, there is no DM-related energy for parallel spins (central row). **c** Anisotropic symmetric exchange: the spin pair tries to align along a preferred axis (in other words, the symmetric anisotropic exchange is a form of "two–site anisotropy")

- the Heisenberg term is usually much larger than the other two terms (DM and Kitaev-like); the latter, in fact, can be considered in many cases as small perturbations on top of the main scalar coupling;
- as Moriya showed, [21] the functional form of DM- and Kitaev-like terms can be obtained via a second-order perturbative approach of the SOC term between two sites within an Anderson superexchange formalism. Both the DM and symmetric-anisotropic interaction terms are therefore rooted within SOC; in closer detail, DM is first-order in the SOC constant ξ and the symmetric anisotropic exchange is quadratic in ξ;
- the detailed form of the DM and symmetric-anisotropic exchange depends on the crystal symmetries. For example, DM is zero if there is an inversion center in the local atomic environment describing the spin-pair and the ligands; other so-called "Moriya rules" [24] are very often used to infer from symmetry *i)* whether DM is at all allowed; *ii)* the direction of the DM vector;
- the spin-Hamiltonian in Eq. 5 is the simplest expression possible, as it only contains bilinear terms in the spin coordinates. Although this is generally a good approximation, higher order terms (such as biquadratic [25] or fourth-order four-spin interactions [26]) are sometimes needed to carefully describe the exchange interactions of complex systems.

As mentioned, the DM antisymmetric exchange gives rise to spin non-collinearity (*i.e.* canted antiferromagnets, spin-spirals), non-coplanarity and other unusual spin-configurations. We, therefore, take here the opportunity to review the more common non-collinear spin-textures that occur in complex magnets (see Fig. 3). Spin-spirals are periodically modulated spin configurations, where the spins of neighboring magnetic moments rotate uniformly around a particular direction as a function of position. They can be characterized by a propagation vector **q** and by the plane in which the

spins rotate. Spin spirals can be divided into two classes: (i) spin cycloids, where the spins rotate in a plane containing **q**; (ii) spin helices (or proper–screw), where the spins rotate in a plane perpendicular to **q**. Furthermore, as DM is the driving force behind the formation of skyrmions, [27, 28] we mention that the latter are small magnetic vortices, in which the orientation of magnetic spins twists around a central core (cfr Fig. 3b) for a skyrmion lattice). These structures are characterized by a non-zero topological charge, which makes them topologically protected and extremely stable; moreover, they can move through the hosting magnetic material with low energy consumption. These complex spin-textures attracted in the last couple of decades hectic interest [29, 30] from (i) the fundamental point of view, in terms of, for example, topologically non-trivial spin-textures (not only skyrmions, but also merons—cfr Fig. 3c) for a merons lattice -, antiskyrmions, etc); (ii) the applicative point of view, in terms of, for example, skyrmion race track memory and low-power spintronic devices.

2.3 Spin–orbit coupling in non-magnetic materials

Even in solids that do not show long-range magnetic order, the spin degree of freedom can become "active" and SOC can there drive many interesting phenomena, as detailed below:

2.3.1 Peculiar effects in materials band structures

SOC often produces band splittings at (or close to) high-symmetry points in the Brillouin zone. For example, in standard elemental semiconductors, such as Si or Ge, the valence band maximum, mainly formed by p orbitals and located at the Zone center Γ, is three-fold degenerate, when neglecting relativistic SOC. Upon including the latter, there occurs a level splitting into a two-fold degenerate level, characterized by two different curvatures away from Γ (dubbed as "heavy-hole" and "light-hole" bands, referring to the relation between effective mass and bands curvature) and a singly degenerate level (labeled as "split-off" band). The splitting magnitude between singlet and doublet increases with the atomic number of the atom whose p orbitals form the valence band maximum (for example, one observes a larger splitting in Ge than in Si).

Things become much more intriguing when considering the action of SOC in the band structure of systems where inversion symmetry is broken. Indeed, if we apply space inversion symmetry (SIS), an electron moving with linear momentum **k** changes into **-k**, with the spin unchanged; on the other hand, if we apply time reversal symmetry (TRS), a particle moving with linear momentum **k** changes into one moving with **-k**; reversing time will also invert the precessional motion of the electron, so by this classical analogy, one can infer that its spin is reversed in sign. The following relations on the band structure eigenvalues for the up- and down-spin channels (labelled by $\uparrow$ and $\downarrow$, respectively) are then imposed by symmetry, when SIS and TRS are preserved:

$$SIS \rightarrow \varepsilon_{\mathbf{k},\uparrow} = \varepsilon_{-\mathbf{k},\uparrow} \tag{6}$$

$$TRS \rightarrow \varepsilon_{\mathbf{k},\uparrow} = \varepsilon_{-\mathbf{k},\downarrow} \tag{7}$$

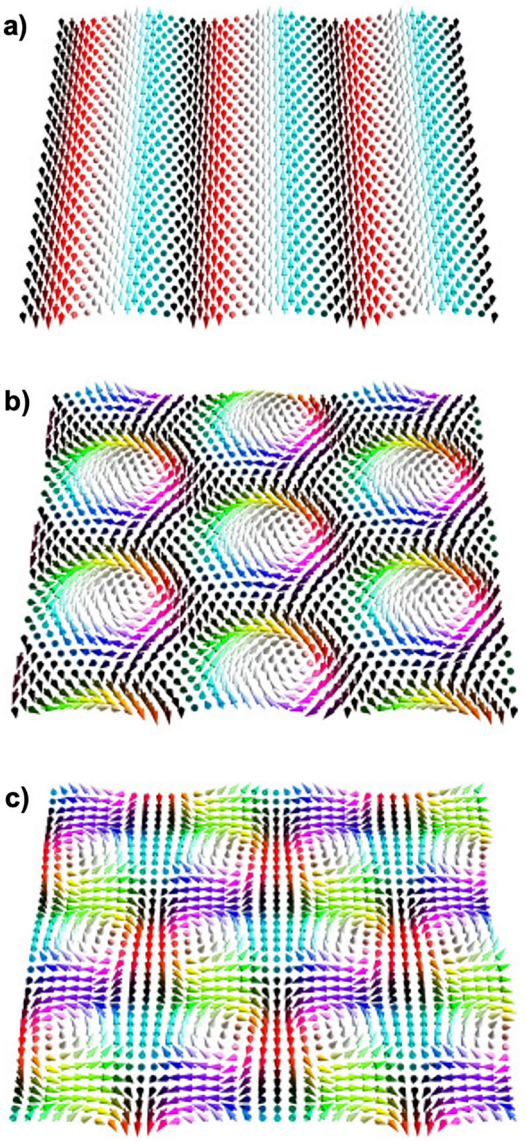

Fig. 3 Some of the most common non-collinear and non-coplanar spin textures: **a** spin helix; **b** skyrmion lattice; **c** meron-antimeron lattice. The colors of the arrows denote different in-plane spin projections. Adapted from Ref. Göbel et al. [30]

Let us now discuss, on the basis of these relations, what happens to the (spin-resolved) band structures, when we remove either SIS or TRS. For simplicity, we start with a free-electron parabolic band structure. In the presence of both TRS and SIS (Fig. 4a), both Eqs. 6 and 7 hold, so there is no spin-splitting at any **k** point; in other words, the band structure is double-degenerate for spins at all **k**-points. In the presence of SIS, but by breaking TRS (Fig. 4b), Eq. 6 holds but Eq. 7 does not hold, so there is a spin-splitting at all **k** points; this is what usually happens if an external magnetic field is applied or if the material shows long-range ferromagnetic order. More

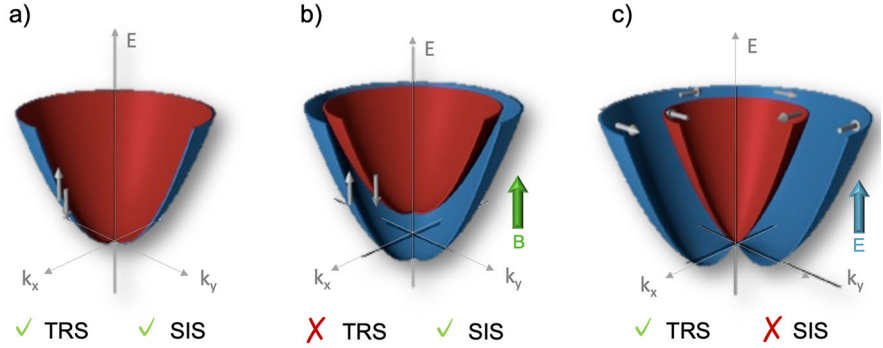

Fig. 4 Schematic spin-resolved band structure plot: horizontal axes denote the k_x and k_y directions in the BZ, the vertical axis denotes energy E. **a** Upon preserving both TRS and SIS, the band structure is double-degenerate with respect to the spin degree of freedom, *i.e.* no spin-splitting is present. This follows from the symmetry-imposed relation: $\varepsilon_{\mathbf{k},\uparrow} = \varepsilon_{-\mathbf{k},\uparrow} = \varepsilon_{-\mathbf{k},\downarrow}$ **b** Upon preserving SIS but breaking TRS, the band structure shows a Zeeman-like spin-splitting. This follows from the symmetry-imposed relation: $\varepsilon_{\mathbf{k},\uparrow} = \varepsilon_{-\mathbf{k},\uparrow} \neq \varepsilon_{\mathbf{k},\downarrow}$. **c** Upon preserving TRS but not SIS, the band structure shows a k-dependent spin-splitting according to the Rashba effect. This follows from the symmetry-imposed relation: $\varepsilon_{\mathbf{k},\uparrow} = \varepsilon_{-\mathbf{k},\downarrow} \neq \varepsilon_{\mathbf{k},\downarrow}$. Gray arrows represent the spin-expectation values; the vertical green arrow and blue arrow in panels **b** and **c**, respectively, label the magnetic and electric field, respectively

unconventionally, a spin splitting is allowed to occur, at least by symmetry, even in the case when TRS is preserved (*i.e.* no magnetic order, no applied magnetic field), but SIS is broken (Fig. 4c); in this case, Eq. 7 holds but Eq. 6 does not hold, so a **k**-dependent spin-splitting is symmetry–allowed.

We remark that SOC by itself is unaffected by breaking TRS (as both **l** and **s** change sign upon time-reversal, but their scalar product does not) or SIS (neither **l** nor **s** change sign for SIS breaking, so that their scalar product also does not). However, when SOC is combined with some of the above–mentioned symmetry restrictions, the following SOC-driven effects emerge:

- **Rashba and Dresselhaus effects**. In the absence of inversion symmetry, spin–orbit coupling can give rise to an effective magnetic field, $\mathbf{B}_{eff}$ (Lorentz transformation of an electric field **E**), even in non-magnetic materials, and therefore, to a **k**-dependent spin-splitting in the electronic structure, in proximity to high-symmetry points of the Brillouin Zone. The effect is usually expressed in terms of the Rashba–Bychov Hamiltonian [31]:

$$H_R = \alpha_R \, \sigma \cdot (\mathbf{k} \times \mathbf{E}) \tag{8}$$

  It induces the so-called Rashba effect (RE), [32, 33] α_R being the Rashba coefficient. The effect is schematically illustrated in Fig. 5, where - similarly to Fig. 4c - a free-electron-like parabolic band structure is taken as unperturbed situation, on top of which acts the Rashba Hamiltonian, giving rise to a linear-in-**k** shift of the bands. In addition to the bands, in Fig. 5a the spin-texture (*i.e.* the spin-expectation value calculated over each wavefunction) is also shown: one observes the so-called "spin-momentum locking", with the spin perpendicular to linear momentum and

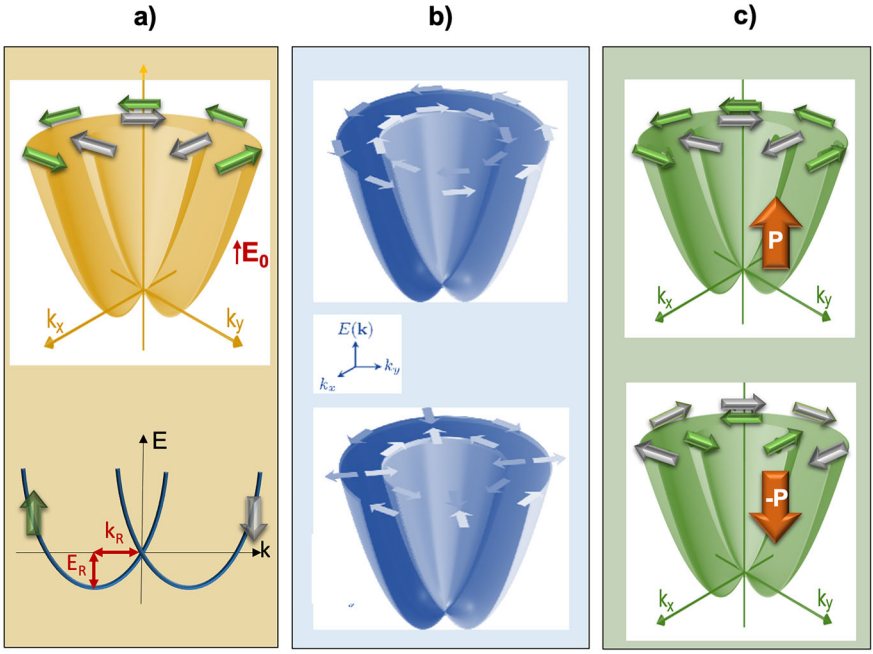

Fig. 5 **a** Rashba effect: parabolic band structure linearly shifted in momentum with respect to the high-symmetry point, in the presence of an electric field $\mathbf{E_0}$ (directed along the vertical z-axis) and of SOC. Green and gray arrows denote spin textures. Lower panel: band dispersion along a specific direction in the BZ. Highlighted are k_R (shift of parabolas in momentum space) and E_R (difference in energy of the minimum of the band with respect to the point where the two linearly shifted parabolas cross. **b** Different spin-textures for Rashba effect (upper panel, polar space groups) and Dresselhaus effect (lower panel, non-centrosymmetric non-polar space groups). **c** FERSC concept: Rashba effect in a ferroelectric material in the presence of SOC. The FE polarization **P** (shown by an orange arrow) is directed along the vertical axis. Upper and lower panels show states with opposite ferroelectric polarization. When switching the direction of polarization (via an electric field), the spin texture switches (see oppositely directed orange arrows)

to the electric field. As for the Dresselhaus effect, [34] we note that is not unambiguously defined in the past literature. Originally, it was interpreted as an effect occurring in bulk materials when Bulk Inversion Asymmetry (BIA) is present, at variance with the Rashba effect occurring at surfaces/interfaces, where Surface Inversion Asymmetry is present. The Dresselhaus term is derived to induce a spin splitting proportional to k^3 (at variance with the linear-in-**k** dependence of the Rashba effect); as such, the Dresselhaus splitting is rather small in the relevant region around Γ. However, it was then realized that the Rashba effect can occur, in addition to surfaces, also in *bulk* polar materials: a pioneering paper [35] by Tokura and collaborators unambiguously showed, both theoretically and experimentally, that bulk BiTeI is characterized by a bulk Rashba effect (*i.e.* without the presence of a surface). More recently, according to Zunger et al. [36] the Dresselhaus effect was defined as occurring in *non-centrosymmetric, but non-polar structures*, such as zincblende GaAs, InSb, etc. It produces a band dispersion very similar to that driven by the Rashba effect, but with a different spin-texture (cfr Fig. 5b). In fact,

the Dresselhaus effect can lead to radial spin textures along some specific symmetry directions in k-space (*i.e.* the spin expectation value for a certain state at a momentum **k** is directed parallel to **k**), at variance with the Rashba effect where the spin-texture is always tangential (*i.e.* the spin expectation value for a certain state at a momentum **k** is directed perpendicular to **k**).

- **Rashba effect in ferroelectrics**. Ferroelectrics [37] are a class of materials showing a permanent electric polarization **P** (*i.e.* dipole per unit volume) below a critical Curie temperature; in other words, ferroelectrics undergo a phase transition, for which polarization is the order parameter. Bistability is a characteristic of ferroelectrics: not only the presence of an electric dipole is necessary, but the electric polarization has to be switchable by the application of an opposite electric field. More generally, the electric polarization shows an hysteresis cycle in the **P-E** space, much in the same way as a magnetization in ferromagnets shows an hysteresis cycle in the **M-H** space. We here recall our discovery made in 2013 of a new class of functional materials, called Ferroelectric Rashba Semiconductors (FERSC) [38, 39]. As already noted, the Rashba effect can occur in polar bulk materials. Later on, the first example of bulk RE in a FE material, GeTe, was proposed by our group [38]. In fact, SIS breaking is a condition intrinsically satisfied in ferroelectrics, which by definition show a polar axis. In GeTe, we showed that the Rashba splitting is as large as 270 meV. More importantly, we predicted the spin-texture to switch by switching P, as shown in Fig. 5c), where opposite directions of FE polarization lead to opposite spin-expectation values. This is a consequence of the changing sign in the Rashba interaction when reversing the electric field (that switches polarization), thereby allowing the non-volatile control of the spin texture by means of the electric field. Our predictions gave rise to subsequent experimental confirmations by means of Angle Resolved Photoemission Spectroscopy, [40] to the related room-temperature spin-to-charge conversion process (of interest for spin–orbitronics) [41] and to the flourishing of a "FERSC-focused subfield".
- **Spin-Valley Coupling**. Let us start with the definition of "pseudospin". Although the spin represents the quantized intrinsic angular momentum of a particle, several other physical attributes can mimic a spin-1/2 behavior and they are generally labeled as "pseudospins". Examples include the layer index in van der Waals bilayers, [42] the two hyperfine split states in cold-atoms, [43] Nambu pseudospins in superconductors, etc. which are all identified as good quantum numbers to explain specific physics phenomena. A pseudospin can be described as a superposition of two quantum states and in terms of Pauli spin matrices for spin-1/2, $\boldsymbol{\sigma} = (\sigma_x, \sigma_y, \sigma_z)$. In materials with hexagonal/honeycomb lattices (cfr Fig. 6a), lacking inversion symmetry and containing heavy elements (such as semiconducting monolayers of $4d$ or $5d$ transition metal dichalcogenides), Xu et al. [44] one can introduce the so called "valley pseudospin", referring to band edges located at specific high symmetry points different from Γ (for example at the corners of the hexagonal Brillouin zone, K and K', see Fig. 6b), generally labelled as "valleys". In these systems, there can be a spin–valley coupling leading to a spin–orbit-induced Zeeman-like spin-splitting for band edges located at K and K'; in fact, the latter are non-Time- Reversal Invariant Momenta, where the Kramers theorem does not hold and spin degeneracy is allowed to be broken. In this case, the dis-

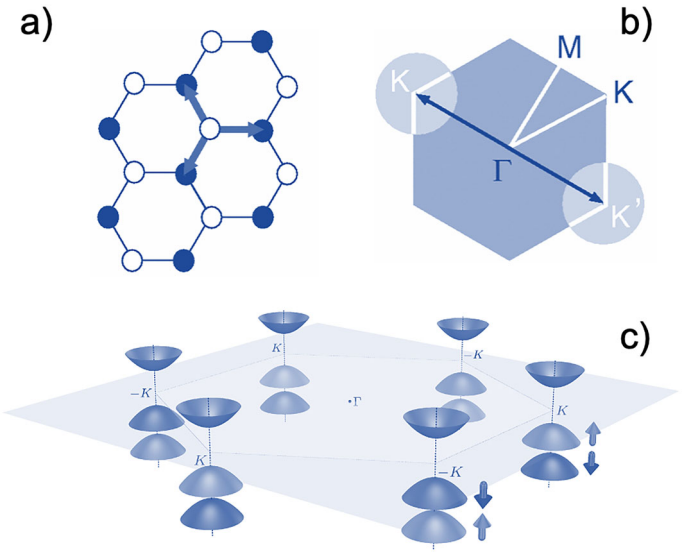

Fig. 6 **a** Honeycomb lattice, with two different atomic sites (empty and filled circles). **b** Brillouin zone of the hexagonal lattice, with opposite corners, K and K' (or $-K$), highlighted by circles. **c** Typical band dispersion (valence band maximum and conduction band minimum) of transition-metal dichalcogenides around the K and $-K$ valleys, presence of band-gap and Zeeman-like spin–orbit induced splitting at the valence band top

persion for spin-split bands around K looks like a Zeeman Spin-Splitting (ZSS): $E_{\pm}(k) = (\hbar k^2/2m^*) \pm \alpha\Delta_Z$ As shown in Fig. 6c, the spin-expectation value of the valence band maximum at K (say, up-spin) is opposite to that at K' (say, down-spin). This kind of pseudospin can be, therefore, used to store information and is at the heart of the so-called "valleytronics", of great promise due to the reduced back–scattering (as mentioned, K and K' showing different spin-related properties).

2.3.2 Topological condensed matter

Let us first note that it is not the aim of this review to cover the broad and active field of topological insulators (TIs), Weyl semimetals, topological superconductivity, etc and we rather refer the reader interested in these topics to specific reviews [45–49]. At the same time, SOC is so crucial in this area that one cannot overlook its relevance in a SOC-devoted review. For the sake of brevity and in the spirit of the review, we will only focus on the role played by SOC, which is clear already from the main concepts underlying the Quantum Spin Hall effect and topological Insulators, *i.e.* among the first basic concepts introduced in the field of topological matter.

As we reflect on several pivotal observations in the field of topological condensed matter, it becomes apparent that SOC serves as a "built-in magnetic field" within non-magnetic materials. Indeed, SOC acts analogously to the applied magnetic field in the quantum Hall effect (QHE), as discovered by Thouless et al. [50] where one

observes quantized Hall conductance plateaus and the conductivity at the edge of a two-dimensional electron gas is characterized by the topological Chern number. For example, the topological quantum Hall state occurs for electrons confined within a two-dimensional interface between two semiconductors in a strong magnetic field. The analogy between applied field and SOC is, however, valid when considering just one type of spin; in fact, for particles having opposite spin, SOC acts as a magnetic field with opposite direction. In heavy atoms, the spin–orbit field is strong because the electrons move at relativistic speeds and they feel an intense spin- and momentum-dependent force. Indeed, the effects on opposite electron spins do not cancel one with the other, but rather give origin to a new phenomenon, the quantum spin-Hall (QSH) effect [51, 52] in TIs. As shown in Fig. 7a, all the electrons of one spin direction circulate in one way, while all the electrons with opposite spin circulate in the opposite way, resulting in a total orbital current. In the bulk of the material, this current is difficult to detect, however, on the boundary it results in quantized spin conductivity. In QSH insulators, there occurs the so-called “band inversion", *i.e.* the valence sub-band maximum lies energetically above the conduction sub-band minimum; due to the interaction between valence and conduction sub-bands, a gap opens. As such, in QSH materials, the bulk remains insulating, but the bulk band gap closes at the edge, where two 1D conducting channels occur, with SOC granting an odd number of helical pairs at each edge. In the end, the two conducting channels counter-propagate and carry opposite spin, so as to form a helical spin-pair wrapping around the edges. In addition, we note that: (i) at variance with the QHE, no applied magnetic field is needed in QSH insulators; (ii) the presence of edge modes is protected by time-reversal symmetry (preserved by SOC); (iii) the backscattering is strongly suppressed, as scattering in a state with opposite momentum requires jumping on the opposite edge upon preserving the spin direction. This results in what is commonly referred to as “dissipationless" transport through the edge states: electrons travel without scattering, thereby avoiding energy loss as heat.

The 3D topological insulators (of which Bi_2Te_3, [53] Bi_xSb_{1-x} [54] are prototypical materials) are an extension of this 2D QSH situation (see Fig. 7b). Rather than conducting 1D channels, as in the QSHE, there are metallic Dirac-like massless surface states, characterized by spin-momentum locking (*i.e.* the spin is perpendicular to the corresponding **k** vector). As for 2D QSH insulators, SOC plays here the role of a spin- and momentum-dependent magnetic field.

2.4 Spin–orbit coupling in multiferroic materials

Multiferroics are materials showing at the same time one or more of the following ferroic long-range orders: magnetic (spontaneous order of spins), ferroelectric (spontaneous order of electric dipoles) and ferroelastic (spontaneous deformation). In closer detail, multiferroic (MF) materials showing both a spin and dipolar electric order have been under the spotlight in the last two or three decades [56–59]. SOC is a particularly important ingredient when it comes to the so–called “type-II" multiferroics, [60] *i.e.* those materials where the breaking of inversion symmetry and the emergence of a polar axis is brought about by the occurrence of a magnetic phase transitions. In other words, the FE polarization is a *secondary* order parameter of the phase transition,

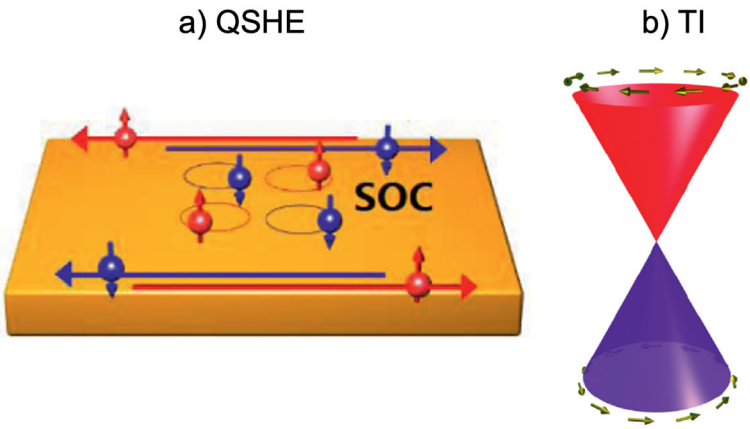

Fig. 7 **a** Quantum Spin Hall effect, showing edge modes as helical spin pairs. Down-spin electrons (in blue) propagate clockwise, upspin electrons (in red) propagate counterclockwise **b** Massless Dirac-like dispersion of the surface states with spin-momentum locking in a topological insulator. Red (purple) cones denote the conduction (valence) band, showing linear dispersion and giving rise to surface/edge states. Adapted from Ref. Wang et al. [55]

induced by the leading *primary* order parameter, which is of magnetic origin. To clarify the concept, let us consider, for example, a paramagnetic to AFM transition below a certain critical temperature. If the spin-order pattern lacks inversion symmetry (as for example in the case of a spin cycloid or a spin helix), the magnetic transition paves the way to the emergence of ferroelectric polarization, occurring simultaneously at the magnetic transition temperature. This was clearly observed in $TbMnO_3$ in a landmark paper for "type-II multiferroics" [61].

Since orthorhombic manganites have been the prototypical class of materials with SOC-driven spin-induced FE polarization, we will discuss this phenomenon in the specific case of $RMnO_3$ (where R is usually a rare-earth ion or Y or Bi). As shown in Fig. 8a, $RMnO_3$ show a *distorted* perovskite crystal structure: at variance with the pristine (*i.e.* undistorted) ABO_3 cubic perovskite, with A sites on the corners of a cube and B-sites octahedrally coordinated by oxygen anions, in ortho-manganites the usually small size of the R ionic radius leads to the so-called "$GdFeO_3$-type" distortions, which tilts the oxygen octahedra, reduces the B-O-B angle with respect to the ideal value of 180° and leads to orthorhombicity. In the absence of magnetic order, the Dzyaloshinskii-Moriya vectors are staggered between nearest neighbors, *i.e.* they alternate in sign so that $D_{12} = -D_{23}$ (cfr Fig. 8c), according to Moriya rules [24]. Here, the equal size is due to the same Mn-O-Mn angle in the high-temperature non-magnetic phase. However, the spin cycloid magnetic order (cfr Fig. 8b) that sets in below the ordering temperature $T_N \sim 30$ K, gains energy for the same orientation (*i.e.* not-staggered) of the DM vectors. Since the size of the DM vector is proportional to the Mn-O-Mn bond angle, this energy lowering mechanism leads to unidirectional displacements (cfr Fig. 8c), where small vertical arrows on top of oxygens show the spiral-induced polar displacement) of the anions, leading to a net polarization. By changing the helicity of the cycloid (*i.e.* for the spins rotating clockwise or counter-

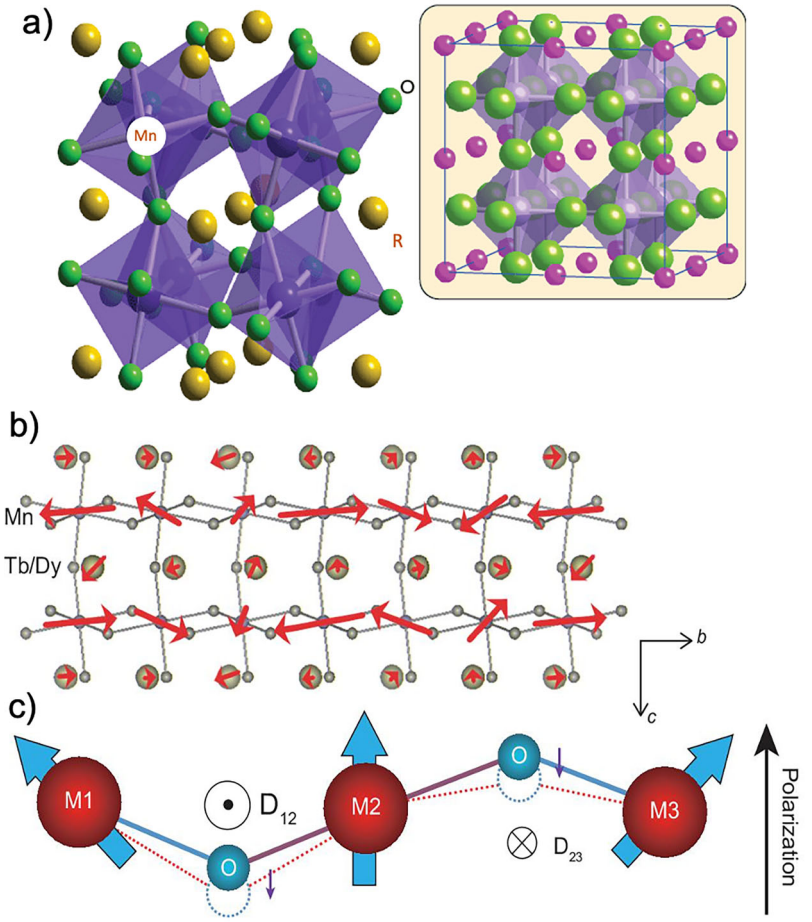

Fig. 8 **a** Distorted perovskite structure of $RMnO_3$ (R denotes a rare-earth ion), showing $GdFeO_3$–like distortion (all the nearest–neighbors Mn-O-Mn angles are bent, *i.e.* reduced from 180°). The ideal undistorted perovskite is shown in the inset on the upper right of the panel (all the nearest neighbors Mn-O-Mn angles are straight, *i.e.* equal to 180°). **b** Spin-cycloid order of Mn magnetic moments, with spins propagating along the b axis and rotating in the $b - c$ crystallographic plane (see arrows located on Mn ions). Spins on the rare-earth (R = Tb, Dy) are also shown for completeness. **c** Distortion of the oxygen upon "inverse DM-mechanism". M1, M2 and M3 denote three neighboring Mn atoms, with superimposed arrows representing cycloidally modulated spins. D_{12} and D_{23} represent the staggered direction of DM vectors between neighboring spins (lying perpendicular to the Mn-O-Mn bonds). The solid lines represent the bonds connecting Mn and O at high temperature; when the cycloidal spin–order sets in, all the O move along the same direction (in this case, they move "down", as shown by the dotted lines denoting the distorted Mn-O bonds), thereby inducing a vertical ferroelectric polarization (see arrow on the rightside). Adapted from Ref. Dong et al. [62]

clockwise, as the spiral propagates along neighboring Mn sites), the polarization can be accordingly switched. This mechanism is often referred to as "inverse DM". In fact, in the presence of a spin spiral, following Sergienko and Dagotto [63], one can use

the following Hamiltonian:

$$H = (\zeta \mathbf{e}_{ij} \times \mathbf{d}_o) \cdot (\mathbf{S}_i \times \mathbf{S}_j) + \frac{2\kappa}{d_o^2} \tag{9}$$

where ζ is a coefficient, $\mathbf{e}_{ij}$ is the unit vector pointing from site i to site j, $\mathbf{d}_o$ is the displacement of oxygen with respect to the middle point of sites i and j. In Eq. 9, the second term represents the elastic energy, with κ labelling the stiffness. The energy is minimized for $\mathbf{d}_o = -\frac{\zeta}{\kappa}\mathbf{e}_{ij} \times (\mathbf{S}_i \times \mathbf{S}_j)$. As such, in the presence of a spin spiral, all the oxygens move in the same direction (which reverses upon switching the spiral helicity).

In parallel to this "displacive" mechanism, there exist also a purely electronic mechanism. In fact, SOC can modify the electron cloud around magnetic ions, when dealing with non-collinear spin pairs, resulting in a purely electronic charge dipole. This phenomenon was discussed in terms of spin-currents by Katsura, Nagaosa, and Balatsky and it is, therefore, known as the "KNB theory" [64]. The authors employed quantum perturbation theory on the Hubbard model incorporating spin–orbit coupling. According to the KNB model, the induced charge dipole is directly proportional to $\mathbf{P} \sim \mathbf{e}_{ij} \times (\mathbf{S}_i \times \mathbf{S}_j)$. A similar derivation can be carried out via a phenomenological model based on the Landau free energy [65]. Both the KNB model and the Sergienko-Dagotto model were largely used in the context of type–II multiferroics, as they can be considered as equivalently valid, occurring at the same time, both induced by non-collinear spin-textures, the first involving a purely electronic mechanism and the latter involving ion displacements.

A final word on the following question: why this SOC-induced mechanism is often called "inverse DM"? A kind of hand-waving argument is the following: one can think that "direct" DM occurs when inversion symmetry is broken and it produces spin–canting, When "inverse" DM occurs, one starts from canted spins and, as a result, inversion symmetry is broken (and FE polarization emerges).

3 Additional recurring concepts in the physics of complex materials

Before moving to the discussion of selected first-principles results showing the relevance of spin–orbit coupling in complex materials, let us report a few concepts that are not strictly or uniquely related to SOC, but they are of relevance to understand the results that will be presented later on.

3.1 Exchange frustration

Frustration in exchange-coupled systems with classical spins often leads to unconventional spin textures, emergent phenomena (such as unconventional spin-transport) and complex phase diagrams, therefore, attracting huge interests of the community working in complex magnetism. We refer the reader interested in the field of frustrated magnets to a few specialized references, Lacroix et al. [66] and Normand [67] while here we only recall some very general concepts.

The term “frustration" was first introduced for spin-glasses and refers to a system in which it is impossible to satisfy at the same time all the exchange interactions at play. In other words, there is no simple spin pattern that minimizes the energy: competing exchange interactions result in frustrating a uniform magnetic order. A paradigmatic example of exchange frustration is an equilateral triangle with AFM exchange. When placing two spins in an AFM configuration, the third spin in the triangle cannot be arranged in a collinear way without making “unhappy" one of the bonds (that would both like to be AFM-coupled). Indeed, the classical ground state of this textbook-case shows non-collinear spins oriented at 120° one relative to the other. One interesting consequence of this simple example is that, to have frustration one needs at least one interaction to be AFM. In fact, if all the interactions are FM, clearly the ground state is the one where all the spins are parallel. However, even when all the interactions are AFM, not necessarily one observes geometrical frustration. Indeed, for any bipartite lattices (*i.e.* where the lattice can be separated into two interpenetrating sublattices, such as square or honeycomb lattice) in which each spin of one sublattice is AFM-coupled to the neighboring spins of the other sublattice, the simple “unfrustrated" Néel state is the ground state: one sublattice shows spin–up and the other sublattice shows spin–down. A necessary but not sufficient condition to have geometrical frustration is to have AFM exchange interactions in loops of odd size (triangle, pentagons, etc). One observation that has already emerged so far is that frustration is strongly linked to the underlying lattice. It would, therefore, be more appropriate to speak about “geometrical frustration", happening in certain kind of lattices (such as triangular or kagomé in two-dimensions and pyrochlore in three-dimensions). We finally remark that frustration markedly differ in classical spins with respect to quantum spins. At zero temperature, classical spins have no further available degrees of freedom for optimizing the potential energy (in addition to the classical pair-wise spin Hamiltonian); as such, the physics of frustrated systems results in either compromise spin-textures (canted spins, spin spirals, etc) or highly degenerate manifolds of equally frustrated states. In contrast, quantum spins have alternative ways to optimize the energy, related to their intrinsic zero-point fluctuations (which could be therefore regarded as “kinetic" in origin). For the sake of simplicity, we will deal only with examples, involving triangles or spin-chains where the classical ground state is complex (*i.e.* non-collinear or non-coplanar), but neglecting any quantum fluctuation.

3.2 Berry-phase approach to ferroelectric polarization

The evaluation of the electric dipole of a finite system is straightforward, using the expression $\mathbf{D} = \int \mathbf{r}\, \rho(\mathbf{r})\, d\mathbf{r}$, where $\rho(\mathbf{r})$ is the charge density. On the other hand, determining the electric polarization in crystalline solids poses challenges due to periodic boundary conditions. This issue was addressed roughly three decades ago and solved by the groups of King-Smith and Vanderbilt [68] and Resta [69] with the introduction of the so–called “modern theory of polarization". This theory clarified that the electric polarization in a crystalline solid manifests as a *polarization lattice* rather than a vector. The total polarization for a given crystalline structure comprises ionic and electronic contributions: $\mathbf{P} = \mathbf{P}_{ion} + \mathbf{P}_{el}$ The ionic contribution originates from the

nucleus and core electrons and is expressed as $\mathbf{P}_{ion}=\frac{e}{\Omega}\sum_i Z_i \mathbf{r}_i$, where Ω is the volume of the unit cell, $\mathbf{r}_i$ denotes the ionic position in the unit cell, and Z_i is in modulus equal to the number of valence electrons of each i-th ion. The electronic contribution is then expressed as a Berry phase term:

$$\mathbf{P_{el}} = -\frac{ie}{2\pi^3}\sum_{\sigma,n}^{occ}\int_{BZ} d^3\mathbf{k}\left\langle u^{\sigma}_{n,\mathbf{k}}\middle|\frac{\partial u^{\sigma}_{n\mathbf{k}}}{\partial \mathbf{k}}\right\rangle \tag{10}$$

where $u^{\sigma}_{n\mathbf{k}}$ is the periodic unit-cell part of the Bloch function. Upon evaluating Eq. 10, one should check that the system is insulating and that it has the same number of occupied bands for each $\mathbf{k}$ point, otherwise the Berry phase becomes ill-defined. We anticipate that the implementation of Eq. 10 is now a routine feature implemented in most DFT electronic structure codes, as discussed in the following Section.

4 How to estimate spin–orbit-related properties from density functional theory

Density Functional Theory (DFT) [70, 71] is a computational quantum mechanical method used to study the electronic structure and properties of atoms, molecules, and solids. Based on the Hohenberg–Kohn theorems [70] and on the Kohn–Sham equations, [71] DFT provides a framework for describing the behavior of electrons within a system by focusing on the *electron density*, rather than tackling the wave-functions by solving the many-body Schrödinger equation directly. The central idea of DFT is to express the total energy of a system as a functional of the electron density. By minimizing this functional, one obtains the ground-state electron density, on the basis of which various properties of the system can be predicted. DFT calculations typically involve approximations, most notably the exchange-correlation functional, which accounts for the complex exchange and correlation effects between electrons. Various approximate functionals exist, each with its strengths and limitations; the Local Density Approximation (LDA) [71] is one of the simplest approximations for the exchange-correlation energy, assuming that the exchange-correlation energy density at a point in space depends only on the local electron density at that point. Despite its widespread use, DFT has limitations, such as its inability to accurately describe strongly correlated systems and dispersion interactions. These limitations also affect the ab-initio modelling of magnetic materials, where the magnetism is due to correlated $3d$ electrons (or to $4f$ electrons, where correlations are even stronger). In the aim of improving the accuracy of DFT, researchers have developed ways (such as Hubbard-like DFT+U) [72] to describe correlations in magnetic materials with localized spins. In any case, DFT has undoubtedly become one of the most widely used tools in theoretical chemistry, physics, and materials science, due to its balance between accuracy and computational efficiency. It can predict properties such as electronic structure, molecular and crystalline geometries, reaction energetics, etc., thereby enabling researchers to explore complex phenomena and design new materials with tailored properties.

Traditionally, DFT codes neglect SOC due to its computational complexity and only treat relativistic effects via Darwin and mass-velocity terms. However, for systems where SOC plays a crucial role (such as materials with heavy elements, transition metals, etc.), it becomes essential to include SOC in DFT calculations to obtain accurate results. One common method is to incorporate SOC starting from a scalar relativistic approximation within the framework of DFT. SOC is then treated as a perturbation, implementing $H_{SOC} \propto \frac{1}{r}\frac{\mathrm{d}V(r)}{\mathrm{d}r}\ \sigma \cdot \mathbf{L}$, where $\mathbf{L}$ is the angular momentum operator, $\sigma = (\sigma_x, \sigma_y, \sigma_z)$ is the vector of the Pauli spin matrices and $V(r)$ is the spherical part of the potential. In many DFT codes, it is assumed that the predominant contribution comes from the region close to the nuclei and the SOC contribution is only evaluated within spheres centered on the nuclei, neglecting the interstitial contribution. For example, we refer to Steiner et al. [73] for the implementation of SOC within the Vienna Ab-initio Simulation Package (VASP) [74–76] in a Projector-Augmented-Wave (PAW) [77] formalism within the PAW spheres.

We finally mention that there exist DFT codes, mostly used in the chemistry community, where a fully relativistic treatment is explicitly taken into account by solving the full four-component Dirac equation; clearly, these approaches must be adopted whenever the approximation of treating SOC as a perturbation is not valid [78].

In the two subsections below, we present DFT-based methods to estimate SOC-induced properties in the context of complex magnetic materials.

4.1 Total-energy mapping analysis and four-states method for spin-Hamiltonian parameters

In this section, we primarily discuss one technique for estimating spin interaction parameters (such as those appearing in Eq. 5) using ab–initio calculations applied to crystalline materials, with implicit assumptions of periodic boundary conditions, mainly using an approach based on energy-mapping analyses. Before entering into details, we would like to mention that there exist several alternative approaches, such as: (i) the Green's function method, relying on the magnetic-force linear response theory; [79–81] (ii) approaches based on quantum-chemical wave-functions, often used in the chemistry community for non-periodic systems [82, 83].

In an energy-mapping analysis, one performs multiple DFT calculations with various spin arrangements to evaluate their respective total energies. Subsequently, based on the assumed effective spin Hamiltonian, one expresses the total energies corresponding to these spin configurations via specific equations, in terms of several spin-Hamiltonian parameters. By fitting the parameters appearing in the total energy expressions derived from the effective spin Hamiltonian model so as to match the numerical outcomes of the ab-initio simulations, one estimates the values of the spin-Hamiltonian parameters. Often, one performs DFT simulations for many different spin configurations, so as to obtain more equations than the number of parameters to fit. In this case, a least-square fit is performed to estimate the model parameters.

For the sake of clarity, let us consider a specific example with a simple pure-Heisenberg Hamiltonian, written as:

$$H = \sum_{<i,j>} J_1 \, \mathbf{S_i} \cdot \mathbf{S_j} + \sum_{\ll i,j \gg} J_2 \, \mathbf{S_i} \cdot \mathbf{S_j} + \sum_{<\ll i,j \gg>} J_3 \, \mathbf{S_i} \cdot \mathbf{S_j} \tag{11}$$

taking into account first, second and third nearest neighbour exchange interactions (with coupling constants J_1, J_2 and J_3, respectively) between spins $\mathbf{S_i}$, $\mathbf{S_j}$ localized at sites i, j of a hexagonal lattice (cfr Fig. 9). In Eq. 11, the different sums run over different site pairs, denoting first, second, and third nearest neighbours as $< i, j >$, $\ll i, j \gg$ and $<\ll i, j \gg>$, respectively. In the hexagonal framework, every site has $N_1 = 3$ nearest-neighbours, $N_2 = 6$ s nearest-neighbours and $N_3 = 3$ third nearest-neighbours. With reference to the four different spin configurations shown in Fig. 9, that are consistently calculated by DFT, one can express the different total energies as:

$$E_{FM/Neel} = E_0 + (\pm 3J_1 + 6J_2 \pm 3J_3)|\mathbf{S}|^2$$
$$E_{Zigzag/Stripy} = E_0 + (\pm J_1 - 2J_2 \mp 3J_3)|\mathbf{S}|^2$$

where E_0 denotes a "spin-independent" energy term. By solving this linear system (with four total energies and one spin-independent parameter E_0), the three exchange coupling constants J_1, J_2 and J_3 can be determined.

Before moving on, let us note that, in the energy-mapping analyses, a "rigid spin rotation" approximation is employed: this approximation implies that the spin magnitudes remain constant across various spin configurations. However, this assumption does not always hold true; for instance, the magnitude of the spins may exhibit slight (or, possibly, significant) variations between FM and AFM states. The approximation of constant-spin-magnitude is generally valid in the case of systems with localized magnetic moments (for example, insulators with large moments), whereas it can fail when dealing with small moments in itinerant metallic magnets. In this review, our focus is mostly on insulating magnets, so the approximation of considering constant-magnitude spins (irrespective of their direction) is well justified.

Let us now move to the so-called "four-states" method, a specific kind of energy-mapping method [84]. It is now assumed that the effective spin Hamiltonian comprises solely second-order terms, including isotropic Heisenberg, DM interaction, Kitaev-like anisotropic symmetric exchange, and SIA terms (see Eqs. 5 and 3). The spin-Hamiltonian parameters can be determined via first-principles calculations for four specific spin configurations (this is why the method is called "four-states"). For instance, let us consider the exchange parameter $J_{ij,ab}(a, b = x, y, z)$, *i.e.* the element of the exchange tensor, which couples site i with spin along a and site j with spin along b (see Fig. 10). The energy $E_{ij,ab,\alpha\beta}$ (where $\alpha, \beta = \uparrow, \downarrow$) denotes the configuration where the spin i is either parallel or antiparallel to the a direction (if $\alpha = \uparrow$ or $\downarrow$, respectively), spin j is either parallel or antiparallel to the b direction (if $\beta = \uparrow$ or $\downarrow$, respectively) and all spins except i and j remain unchanged in these four states, forming a "reference configuration" or a "spin bath" (typically a low-energy collinear

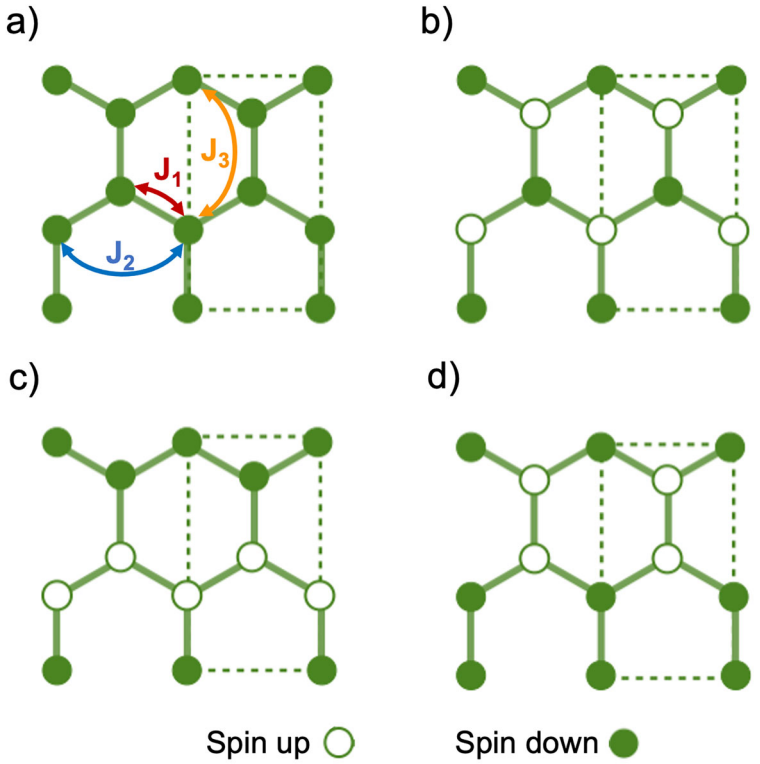

Fig. 9 Four different spin configurations on a hexagonal lattice: **a** FM, **b** AF-Néel, **c** AF-zigzag, **d** AF-Stripy. Empty (Filled) circles denote spin-up (spin-down). In panel **a**, the exchange coupling paths J_1 (red curved line), J_2 (blue curved line) and J_3 (orange curved line) between first, second and third nearest neighbours are also shown. The dashed green lines illustrate the unit cell used to simulate the four different spin configurations

state perpendicular to the $i - j$ plane). Consequently, $J_{ij,ab}$ can be expressed as:

$$J_{ij,ab} = \frac{E_{ij,ab,\uparrow\uparrow} + E_{ij,ab,\downarrow\downarrow} - E_{ij,ab,\uparrow\downarrow} - E_{ij,ab,\downarrow\uparrow}}{4S^2} \tag{12}$$

(S denotes the magnitude of the spin moment on the sites).

In order to estimate the SIA-related parameters, for example $A_{i,ab}$ ($a, b = x, y, z$ with $a \neq b$), one needs to estimate $E_{i,ab,\alpha\beta}(\alpha, \beta = \uparrow, \downarrow)$, *i.e.* the energy of the configuration where spin i is parallel to the direction whose a component is $\pm\frac{\sqrt{2}}{2}$ (for $\alpha = \uparrow$ or $\downarrow$, respectively), the b component is $\pm\frac{\sqrt{2}}{2}$ (for $\beta = \uparrow$ or $\downarrow$, respectively) and the other components are zero. Here, only one spin is aligned along one specific direction, all the other spins in the bath being perpendicular to it.

$$A_{i,ab} = \frac{E_{i,ab,\uparrow\uparrow} + E_{i,ab,\downarrow\downarrow} - E_{i,ab,\uparrow\downarrow} - E_{i,ab,\downarrow\uparrow}}{4S^2} \tag{13}$$

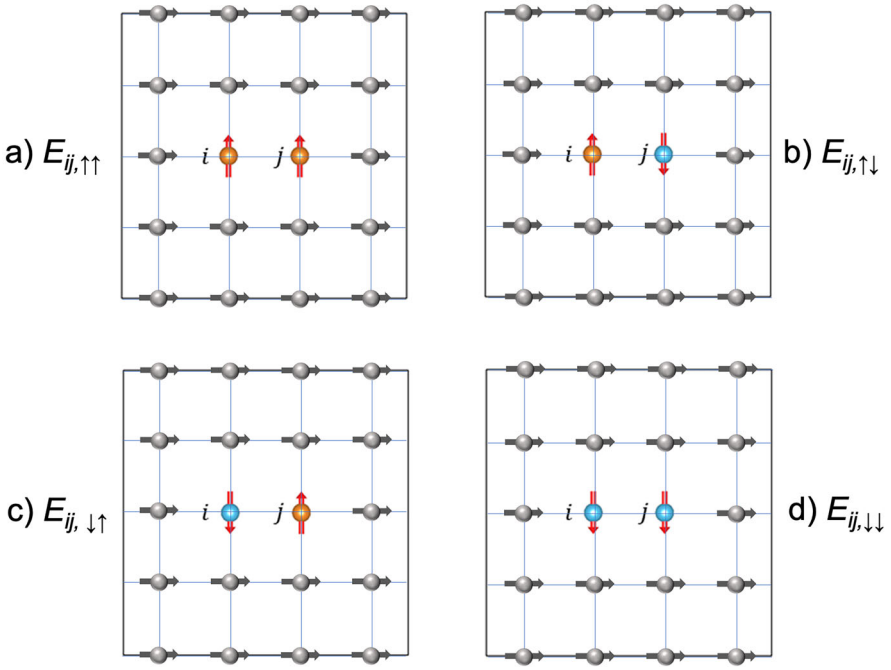

Fig. 10 Schematic representations of the four states used in the four-state method for computing the exchange-constant (here, $J_{ij,yy}$). Spin orientations of the selected spin-couple are represented by orange and light-blue spheres for spins pointing up and down, respectively. All atoms except for i and j are represented with grey spheres, with grey horizontal arrows representing spins (perpendicular to those in the selected i, j couple). The total energies derived from DFT for these four states are labeled as **a** $E_{ij,\uparrow\uparrow}$, **b** $E_{ij,\uparrow\downarrow}$, **c** $E_{ij,\downarrow\uparrow}$, **d** $E_{ij,\downarrow\downarrow}$. Here, we avoided to repeat the yy indices, since they are the same for all the four-states used to evaluate the yy element of the exchange tensor

While the general methodology is the same, for other fine details on how to estimate all the other parameters needed (including for example higher order coupling constants, such as biquadratic exchange), we refer the reader to specific reviews [84–86]. Here, it is important to remark why the four-states method is useful and accurate: it is easy to verify that, with the specific choice of the couple of spins (or of the central spin in the case of SIA), all the other second-order terms involving the interaction between the two spins in the couple and the other spins in the "bath" are exactly cancelled (which is usually not the case when imposing, for example, different AFM patterns in total-energy mapping analyses). In other words, one accurately estimates the exchange constant which couples exclusively two selected spins, without the risk of artificially including other longer ranged exchange constants that can be "effectively remapped" on the exchange constant of interest (this artifact can occur in several cases, see discussion in Ref. [87]).

We stress once more that the exchange-coupling tensor is forced to be diagonal and equal to a constant times the identity matrix in the absence of SOC. In fact, in the latter case, one would simply have a situation in which the Heisenberg model is valid, as spins are isotropic. Any deviations from the Heisenberg model, any anisotropy in the

exchange-coupling paths is therefore due to SOC, giving rise to non-diagonal terms and different terms on the diagonal, microscopically ascribable to DM or Kitaev-like interactions. Similarly, the SIA cannot be evaluated in the absence of SOC. Possible exceptions occur in exotic curved geometries, [88] that go beyond the scope of the present review. In conventional crystalline geometries, the spin degrees of freedom are linked to the lattice (*i.e.* to the real space) only via SOC.

4.2 Magnetoelectric-coupling tensor

Following the discussion of spin-induced polarization in type–II multiferroics (see Sect. 2.4), here we will introduce a DFT-based method that allows the estimate of the electronic part of polarization, as arising from a non-collinear spin arrangement.

Let us examine a spin dimer, representing a pair of neighboring spin sites $\mathbf{S}_1$ and $\mathbf{S}_2$, characterized by spatial inversion symmetry with respect to the midpoint. For simplicity, we'll assume the propagation vector from spin 1 to spin 2 to align with the x-axis. Upon introducing a non-collinear spin configuration in the dimer, the inversion symmetry is broken, consequently triggering the emergence of an intersite spin-induced ferroelectric polarization in the non-collinear spin dimer. According to the general theory of spin-induced polarization, as discussed in detail in Ref. Xiang et al. [89], one can write:

$$\mathbf{P_{12}} = \mathbf{M}(\mathbf{S_1} \times \mathbf{S_2}) \tag{14}$$

where one expresses the magnetoelectric-coupling tensor:

$$\mathbf{M} = \begin{bmatrix} (\mathbf{P}_{12}^{yz})_x & (\mathbf{P}_{12}^{zx})_x & (\mathbf{P}_{12}^{xy})_x \\ (\mathbf{P}_{12}^{yz})_y & (\mathbf{P}_{12}^{zx})_y & (\mathbf{P}_{12}^{xy})_y \\ (\mathbf{P}_{12}^{yz})_z & (\mathbf{P}_{12}^{zx})_z & (\mathbf{P}_{12}^{xy})_z \end{bmatrix} \tag{15}$$

The original KNB model, as explained in Sect. 2.4 and generating an inter-site polarization by means of an "electronic-only" mechanism (*i.e.* no ion displacement is taken into account in the polarization emergence), features $(\mathbf{P}_{12}^{zx})_z = -(\mathbf{P}_{12}^{xy})_y = C$ as the sole non-zero elements of $\mathbf{M}$, with C being a constant. Therefore, the inter-site polarization, as described in Eq. 14, can be understood as a "generalized KNB (gKNB)" model, of which the KNB model is a particular case. Similar to the KNB model, one cannot expect any polarization according to Eq. 15 in the absence of SOC.

The estimate of each element in the tensor of Eq. 15 can be performed by means of DFT in a way which is very similar to the four-state method used for the estimate of the exchange coupling tensor (see previous section): one first constructs a large unit cell, then isolates one specific couple of spins that are set to be perpendicular (say, one spin along x and one spin along y), with all the spins in the bath set to be perpendicular to both spins in the couple. One then evaluates the polarization vector via the Berry phase, as emerging from this spin couple via the gKNB mechanism. By repeating the calculation for all the possible configurations for the two spins in the couple (i) along

x and y, (ii) along x and z, (iii) along y and z, one can then evaluate all the elements in the tensor for that specific couple of spins.

This method reveals as very powerful when dealing with a complex spin texture developing on a spin lattice: the evaluation of the total polarization over all the spin sites in the lattice can be obtained by summing all the contributions coming from each (non-collinear) spin pair in the system, according to Eq. 14 (taking due care in avoiding double-counting terms). Moreover, such an approach based on the magnetoelectric-coupling tensor is extremely convenient when evaluating the polarization arising from a complex spin texture, for which a full DFT (and related estimate via the Berry phase approach) is too expensive from the computational point of view. For example, let us consider the example of a spin spiral propagating along x with long wavelength (say, a periodicity of 30 unit cells), which cannot be simulated within DFT due to the related (too) large magnetic unit cell. To overcome this obstacle, one can describe the spin spiral as composed by nearby spin-dimers, where the angle between two consecutive spins is the same as in the long-wavelength spiral. One can then evaluate via DFT the magnetoelectric-coupling tensor for the specific couple of nearest neighbors and use the tensor to estimate the polarization of the whole spin-spiral as a sum of contributions of polarization coming from the spin-pairs, each spin–couple set to have the same angle as in the spin-spiral of interest. Clearly, the procedure can be adopted in even more complex spin-textures, such as nanometer-scale skyrmions, merons, antiskyrmions, etc where the magnetic unit cell is too large for a full DFT estimate of polarization; still, one can estimate the polarization as arising from the sum of contributions coming from the magnetoelectric-coupling tensor of spin-couples making up the topological spin-textures.

Let us finish this section with a clarification to the reader and a comment on terminology. **M** was used here to label a magnetoelectric-coupling tensor and we have discussed its intersite nature, as inducing polarization due to the non-collinear arrangement of two neighboring spins. One should not confuse this magnetoelectric-coupling tensor with the (much more studied) linear magnetoelectric tensor α (see Ref. [90, 91] and citations therein). In the linear ME effect, which exists in every material where SIS and TRS are broken, a magnetic field **B** induces a first-order electric polarization **P**, and viceversa an electric field **E** induces a first-order magnetization $\tilde{\mathbf{M}}$, as described by:

$$\alpha_{ij}^{ME} = \frac{\partial P_i}{\partial B_j} \| _{B=0} = \frac{\partial \tilde{M}_j}{\partial E_i} \| _{E=0} \tag{16}$$

where the indices i, j denote spatial directions. As such, the linear ME effect does not describe a spontaneous effect (which is described by multiferroicity), but is related to the emergence of magnetization (or polarization) when an external electric (or magnetic) field is applied.

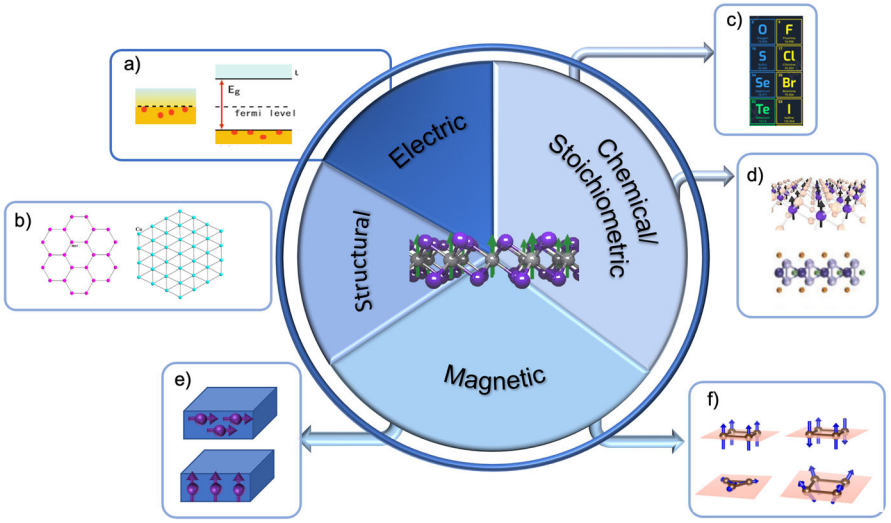

Fig. 11 Variety of properties reported in the class of 2D magnets: **a** electrical properties, with metallic (left panel in the box) and semiconducting/insulating behaviour (right panel in the box); **b** structural, with transition metal atoms arranged in different lattices, such as triangular, honeycomb,…**c** chemical/stroichiometric, 2D-magnets show different anions, such as chalcogenides, halides, etc. and **d** different composition, such as binaries, ternaries, etc. The magnetic properties are also diverse, showing **f** magnetization in-plane or out-of-plane and **g** different spin arrangement, ranging from collinear FM to collinear AFM (upper part of the box), from coplanar to non-coplanar (lower part of the box)

5 Two-dimensional van der Waals magnets

With the boom of graphene, iconically started in 2004 with the first device demonstration, [92] materials science faced a disruptive change. Although archetypal and undoubtedly the most popular, graphene represents just the first example of atomically thin 2D materials, a class of compounds made by self-passivated layers interacting via van der Waals (vdW) interlayer coupling. The weakness of the latter interactions make the engineering of layered heterostructures truly possible, allowing for an easy "LEGO-like" stacking of single sheets, avoiding major limitations imposed by lattice matching or chemical compatibility, typical for conventional 3D systems. About a decade later, the "2D-materials revolution" branched into magnetism: the exfoliation of the first Ising-like compound $FePS_3$ achieved in 2016 [93] and the report of long-range (LR) magnetic order in atomically thin $Cr_2Ge_2Te_6$ [94] and CrI_3 [95] in 2017, launched the field of vdW 2D magnets (2DM).

Phase transitions in 2DM should not be regarded as a new field [96]. Their dawn goes back to 1944, when Onsager [97] first predicted LR magnetic order in an Ising-spin monolayer (ML). This initial kick evolved in the '60 s with the active field of "quasi-2D" magnets, i.e. bulk crystals characterized by a chemical network with a strong 3D-nature (e.g. KNi_2F_4 [98]), though showing anisotropic exchange interactions. In such cases where "crystal-dimensionality" is decoupled from "spin-dimensionality", one observes LR order within specific crystalline planes, along with the absence of

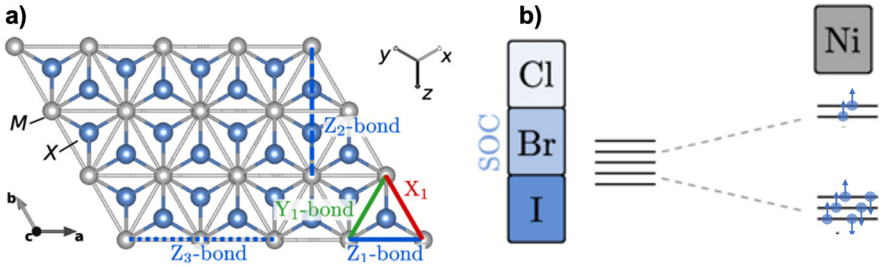

Fig. 12 **a** Monolayer structure of the triangular MX_2 materials (in this paper, M = Ni). Relevant bonds, the global crystallographic (abc) coordinate system and the local cubic (xyz) coordinate system are defined. The bonds (highlighted in blue) labeled as Z_1, Z_2 and Z_3, show the path along which the first, second and third exchange interaction paths develop, respectively. The red X_1 and green Y_1 bonds label symmetry-equivalent first-nearest-neighbour bonds. **b** SOC scale of the ligand: a darker blue color illustrates stronger SOC. On the right-side: Crystal field splitting (CFS) occurring in octahedral Ni and related d^8 electronic filling. The five-fold degenerate free–ion levels are split into three t_{2g} levels (d_{xy}, d_{xz}, d_{yz}) and two e_g levels ($d_{x^2-y^2}, d_{z^2}$). The t_{2g} levels are filled for both majority and minority spin-channels, the e_g are filled only for the majority spin-channel. Adapted from Ref. Riedl et al. [107]

LR spin correlations in the perpendicular direction, due to weak interplanar exchange interactions. The field of low-dimensional magnetism is still very active and continues to address interesting and exotic phenomena, such as spin-Peierls states [99] or spin-liquids, despite low magnetic ordering temperatures that hinder a broad technological impact.

An introductory paragraph to 2D magnetism cannot overlook one of the cornerstones of the field: the Mermin-Wagner theorem [100]. The latter rigorously proves the absence of LR magnetic order in 2D isotropic Heisenberg systems with short-range interactions, due to the role of thermal fluctuations. Importantly, the theorem does not apply as long as any source of anisotropy (*i.e.* SIA or "two-site anisotropy") or LR interactions (*i.e.* dipole–dipole) are present. In this context, clearly the role of SOC appears of paramount importance for spin ordering phenomena in 2D magnets.

Starting from the 1970's, the continuous improvement of thin-film growth techniques and ultra-high vacuum technologies led to 2DM made of "classic" transition metal (TM) atoms, including the first observation of exchange splitting in one ML of Co via ARPES [101]. The field of ultrathin-film metallic TM magnets is absolutely crucial in current technology, boosted by the Nobel Prize in Physics awarded in 2007 to P. Gruenberg and A. Fert for the giant magnetoresistance discovery [3]. The field is still very active and can nowadays lead to large-area ML magnets (e.g. Ref. [102]). However, vdW 2DM offer unique opportunities, mainly thanks to their intrinsically weak interactive nature, that allows for easy stacking, twisting, and heterostructure-building with control down to the ML limit and virtual insensitivity to the substrate. This motivated the ever-increasing attention on many fronts (see the recent reviews) [103–106]. From the materials science point of view, 2DM offer a large and stimulating variety, as illustrated in Fig. 11. They are "chemically rich", ranging from binaries to ternaries, from halides to chalcogenides, etc; they are "crystallographically rich", as they offer different lattices (triangular, honeycomb, etc); they are "electrically rich", as their electrical properties range from metallic to semi-metallic to insulating behaviour.

From the magnetic point of view, they show a wide variety in properties, ranging from easy-plane to easy-axis magnets, from ferromagnets to compounds with peculiar and complex (non-collinear or non-coplanar) spin textures. From the experimental point of view, the characterization techniques are much less mature than "standard tools" (*i.e.* neutron diffraction techniques, conventional SQUID, etc.) used to characterize bulk magnets or even TM metallic thin-films, as the reduced dimensionality and the typical micrometer-scale flake structure of 2DM call for local probes with enhanced sensitivity and spatial resolution. From the point of view of applications, 2DM clearly represent the cutting-edge of spintronics miniaturization and their extreme sensitivity to large electric fields applied across the layers may pave the way to long-sought electrically-controlled spin-based devices with unprecedented performances. From the technological point of view, integrating 2D materials in crucial part of silicon complementary oxide semiconductor (CMOS) chips in the back-end or front-end of the line may allow for beyond-CMOS applications in the so-called "More Moore", "More than Moore" and "CMOS+X" approaches, with an increased sustainability of information technology provided by the drastic reduction of material usage in 2D electronics. As already mentioned, this review is more focused on the basic physics point of view and 2D magnets offer a rich playground: fundamental questions are still unsolved, such as the microscopic origin of 2D-magnetism, its dependence on external stimuli (such as electric/magnetic fields, light, temperature, strain, etc.) or the nature of different exchange mechanisms at play. This motivates our discussion on some of these topics, as reported in the following sections. In the spirit of the review, the choice of topics, effects and phenomena is made according to the role played by SOC, which in vdW 2DM appears to be particularly intriguing.

6 Selected example: the case of 2D transition metal dihalides

In this section, we focus on a selected class of 2D magnets: monolayers of transition metal dihalides NiX_2 (space group $P-3m1$) [105]. There, the Ni ion plays the role of the 2^+ cation and the negatively-charged monovalent anion is $X = $ Cl, Br, I. Upon moving from Cl to Br to I, the atomic number increases, so that SOC-effects are expected to become stronger when going down in the periodic table (*i.e.* from Chlorine to Bromine to Iodine, as shown in Fig. 12b). In their bulk form, NiX_2 are van der Waals magnets characterized by weak interlayer interactions, therefore pointing to the possibility of an easy exfoliation of mono-, bi- or few layers. Ni atoms are octahedrally coordinated (*i.e.* each of them is surrounded by six halogen atoms) and they are arranged in a triangular lattice, with a slight trigonal distortion, as illustrated in Fig. 12a. Being divalent, the Ni electronic filling is d^8, with magnetic moments of $S = 1$ (or, equivalently, 2 μ_B). As shown in Fig. 12b, the octahedral crystal field therefore suggests an insulating state, with a fully-filled majority and minority t_{2g} shells and half–filled majority e_g shell.

In the following subsections, we present some ab-initio results obtained via a realistic DFT modelling of Ni-halides in monolayer form, where SOC plays a crucial role.

6.1 Spin-Hamiltonian and Monte Carlo simulations for NiX_2

The spin Hamiltonian that will be used as reference includes single ion anisotropy terms and pair-wise interactions in tensor form (as explained above in Sects. 2.2.1 and 2.2.2):

$$H = \Sigma_l \mathbf{S_l} \cdot \mathbf{A_l} \cdot \mathbf{S_l} + \Sigma_{lm} \mathbf{S_l} \cdot \mathbf{J_{lm}} \cdot \mathbf{S_m} \tag{17}$$

The SIA term, described in the coordinate system (ab^*c), where b^* is the axis perpendicular to both a and c hexagonal crystal axes (cfr. Fig. 12a), can be well approximated by $H_{SIA} = A_c \Sigma_l (S_l^c)^2$. With respect to the NiX_2 layer, a negative (positive) A_c leads to an easy axis (plane). As such, we assume that the main source of anisotropy for NiX_2 (as well as in many 2D materials) manifests in the energy difference between easy-plane and out-of-plane easy axis, neglecting therefore any anisotropy when spins rotate in the plane of the 2D magnet, expected to lead to a much smaller energy scale. As for the bond-dependent bilinear exchange parameters, one can either keep the ab^*c reference system or resort to the cubic coordinate system (xyz), where orthogonalized axes are oriented approximately along the Ni-X bonds (cfr Fig. 12a). We in fact remark that, due to the slight trigonal distortion, the Ni-X bonds are not exactly perpendicular.

Following the bond-dependent parametrization within the Heisenberg–Kitaev model, [22] each bond is labeled according to the cubic axis orthogonal to it. For example, for the nearest–neighbor Z_1 bond, perpendicular to the z axis (cfr Fig. 12a), one can write the exchange matrix as:

$$J_{lm} = \begin{bmatrix} J & \Gamma & \Gamma' \\ \Gamma & J & \Gamma' \\ \Gamma' & \Gamma' & J+K \end{bmatrix}$$

We remark that the matrix shows a symmetric form, as the NiX_2 monolayer crystalline symmetries include SIS and, therefore, antisymmetric DM terms are not allowed. As shown by the matrix above, there are four independent parameters: the isotropic Heisenberg J, the Kitaev anisotropic exchange K and the off–diagonal terms Γ and Γ'. Alternatively, the interaction can be expressed in a different system taking as reference the ab^*c axes, so that the matrix becomes:

$$J_{lm} = \begin{bmatrix} J_{aa} & 0 & 0 \\ 0 & J_{b^*b^*} & J_{b^*c} \\ 0' & J_{b^*c} & J_{cc} \end{bmatrix}$$

Both approaches are equivalent and can be transformed one into the other by means of the following relations:

$$J = \frac{1}{6}\left(3J_{aa} + J_{b^*b^*} + 2J_{cc} + 2\sqrt{2}J_{b^*c}\right) \tag{18}$$

$$K = \frac{1}{2}\left(-J_{aa} + J_{b^*b^*} - 2\sqrt{2}J_{b^*c}\right) \tag{19}$$

$$\Gamma = \frac{1}{6}\left(-3J_{aa} + J_{b^*b^*} + 2J_{cc} + 2\sqrt{2}J_{b^*c}\right) \tag{20}$$

$$\Gamma' = \frac{1}{6}\left(-2J_{b^*b^*} + 2J_{cc} - \sqrt{2}J_{b^*c}\right) \tag{21}$$

In our modellization, we considered a pair-wise interaction for first (J_1), second (J_2) and third (J_3) nearest–neighbors, assuming longer ranged interactions to be negligible. Moreover, taking NiI_2 as an example, we tested that the tensorial nature of the exchange interaction is only relevant for first nearest neighbors, whereas for second and third nearest neighbors, a simpler "scalar-only" Heisenberg-like coupling term is appropriate. In what follows, therefore, we will report J_1 including Heisenberg, and off-diagonal terms, whereas we will only report the Heisenberg term for J_2 and J_3.

Starting from the spin-Hamiltonian in Eq. 17, we investigated the phase diagram [108] of NiI_2 through Monte Carlo (MC) simulations employing a standard Metropolis algorithm. Hexagonal supercells with periodic boundary conditions, having a lateral size of $L \times L$, served as the simulation environment (in the NiI_2 case, MC calculations were conducted for $L = 24$). Starting from elevated temperatures (T), each temperature point underwent thermalization over 10^5 MC steps, followed by statistical averaging over 5×10^5 steps. As an important outcome, MC snapshots could then be used to image the specific spin-texture at a specific temperature. Moreover, MC simulations allowed the evaluation of the spin-structure factor:

$$\tilde{S}(\mathbf{q}) = \frac{1}{N}\sum_{\alpha=x,y,z}\left\langle\left|\sum_i S_{i,\alpha}e^{-i\mathbf{q}\cdot\mathbf{r}_i}\right|^2\right\rangle \tag{22}$$

Here, $\mathbf{r}_i$ represents the position of spin $\mathbf{S}_i$ and $N = L^2$ denotes the total number of spins within the supercell used for Monte Carlo simulations. The bracket notation stands for the statistical average over the MC configurations. The spin structure factor $\tilde{S}(\mathbf{q})$ offers direct insights into the direction and magnitude of the propagation vectors, as it will be clear from the examples shown below.

To evaluate the topological properties of complex spin phases, the topological charge Q (skyrmion number) of the lattice within each supercell can be estimated as the average $\langle Q\rangle = \langle\sum_i \Omega_i\rangle$, where Ω_i is determined for every triangular plaquette formed by three spins $\mathbf{S_1}$, $\mathbf{S_2}$, $\mathbf{S_3}$ [109]:

$$\tan\left(\frac{1}{2}\Omega_i\right) = \frac{\mathbf{S_1}\cdot\mathbf{S_2}\times\mathbf{S_3}}{1 + \mathbf{S_1}\cdot\mathbf{S_2} + \mathbf{S_1}\cdot\mathbf{S_3} + \mathbf{S_2}\cdot\mathbf{S_3}} \tag{23}$$

Based on the above relation, one can then evaluate the topological susceptibility according to the following formula:

$$\chi_Q = \frac{\langle Q^2\rangle - \langle Q\rangle^2}{k_B T} \tag{24}$$

k_B being the Boltzmann constant.

6.2 Magnetic properties for NiX_2: Heisenberg exchange coupling and symmetric anisotropic exchange

For the sake of brevity, we report in this section only the main results with emphasys on the SOC-induced effects, in the spirit of the review. We, however, refer the reader to Ref. Riedl et al. [107] and Amoroso et al. [108] for a much more detailed analysis and broader discussion on the magnetic properties of transition metal dihalides.

We start our presentation by reporting in Table 1 the values of the spin-Hamiltonian parameters (cfr Eq. 17), obtained by means of the Vienna Ab-initio Simulation Package (VASP) along with the four-states method. In order to better model correlation effects, the so-called "DFT+U" approach was adopted, mimicking Hubbard-like physics for correlated electrons (Ni $3d$ in this case) starting from the bare DFT electronic structure. To estimate via ab–initio techniques the effective Coulomb parameter U, as detailed in Ref. Riedl et al. [107], we used the constrained random-phase approximation (cRPA) method [110]. Our findings reveal a decrease in U as a function of the atomic number of the anion, likely attributed to an increased metal-ligand hybridization. Consequently, the least sizable effective interaction U parameter was obtained for 2D magnets containing anionic p-orbitals exhibiting the strongest hybridization, hence being more delocalized (*i.e.* $5p$ of iodine).

The analysis of the results reported in Table 1 reveals several interesting observations: (i) the first nearest neighbor Heisenberg-like term J_1 is FM and increases from Cl to Br to I; (ii) the Kitaev term is basically absent in nickel-chloride, it is very small in nickel-bromide, but it is definitely large in NiI_2; (iii) off-diagonal Γ_1 and Γ_1' parameters are always negligible, except for the non-zero value in nickel-iodide; (iv) as for longer ranged exchange parameters, the second-nearest neighbor coupling constant J_2 is extremely small, whereas the third nearest neighbor J_3 is quite large. Moreover, J_3 increases upon increasing the atomic number of the anion, likely due to increasingly delocalized nature in going from Cl $3p$ to Br $4p$ to I $5p$ states. The results reported in Table 1 can be well interpreted in terms of Goodenough-Kanamori-Anderson rules [111, 112] and different hopping paths (including SOC-induced spin-dependent hopping), as thoroughly discussed in Ref. Riedl et al. [107]. For the sake of completeness, we note that the U and J_H values used in a different study [108] of ours ($U = 1.8$ eV, $J_H = 0.8$ eV) were different than those used in Table 1. However, the results obtained for the spin–Hamiltonian parameters do not qualitatively change, the quantitative differences being minor. As such, it can be safely concluded that any discussion reported below is valid independently on the U and J_H values, provided the Hubbard parameteres are varied within a physically sound range.

6.3 Complex spin-textures in NiI2: spin-helices and topological antiskyrmion lattice

On the basis of what reported in the previous paragraph as for spin-Hamiltonian parameters, we now concentrate on NiI_2 and note that the magnetic characteristics of the system are governed by: (i) intense magnetic frustration stemming from conflicting nearest-neighbor (J_1) ferromagnetic (FM) and third-nearest neighbor (J_3) AFM

Table 1 Calculated spin-Hamiltonian parameters for NiX_2

	U	J_H	J_1	K_1	Γ_1	Γ_1'	J_2	J_3	A_c
$NiCl_2$	4.57	0.84	−2.9	0.0	0.0	0.0	−0.1	+0.8	0.0
$NiBr_2$	3.90	0.79	−3.9	+0.2	0.0	0.0	−0.1	+1.8	0.0
NiI_2	3.24	0.68	−6.2	+2.2	0.0	−0.1	−0.2	+4.2	+0.4

U and J_H denote the two parameters (Hubbard-like and Hund-exchange, respectively), evaluated with cRPA and used within the DFT + U approach (see first two columns, values in eV). $J_1, K_1, \Gamma_1, \Gamma_1'$ (all values in meV) denote the calculated parameters of the Heisenberg–Kitaev Hamiltonian. J_2 and J_3 denote second and third nearest neighbor Heisenberg exchange coupling. A_c denote the SIA constant (in meV)

exchange interactions; (ii) minimal easy-plane single-ion anisotropy contrasted with strong anisotropic symmetric exchange, both influenced by SOC.

Our Monte Carlo calculations, with parameters derived from DFT as reported in Ref. Amoroso et al. [108], uncover that below a critical temperature of approximately 30 K, the NiI_2 monolayer undergoes a spontaneous transition to one of the following two spin configurations (which are isoenergetic, so equally likely to occur):

- a single-**q** spin-helix (*i.e.* proper-screw) propagating along the Cartesian x-axis, i.e., along the Ni-Ni bond direction, with spins rotating in the perpendicular yz-plane (see Fig. 13a) and a propagation vector about $q/2 \sim 1/8$ in reduced coordinates. The spin-helix is mostly determined by isotropic exchange frustration; in fact, when forming "Ni-chains" centered on a Ni site and developing along each of the six-fold equivalent directions, one finds a FM J_1 and an AFM J_3 (which is the second-nearest-neighbor along the chain). This is a typical manifestation of exchange frustration (in the sense of competing exchange interactions, as discussed in Sect. 3.1), which leads to a non-collinear spin-spiral. The spin-texture of the spin-helix is topologically trivial, *i.e.* when evaluating the topological charge $< Q >$, one always finds a zero value.
- a so-called "triple-**q**" state, *i.e.* a kind of superposition between three combined spin-helices, as illustrated in Fig. 13b). This state is characterized by a triangular lattice hosting antibiskyrmions (denoted here as "A2Sk"), where each antibiskyrmion possesses a topological charge $|Q| = 2$ and a vorticity of $m = -2$ (cfr Fig. 13c). The peak in the susceptibility shows the transition temperature and the topological charge can be taken as order parameter of the transition. The lattice periodicity is defined by wavevectors $\mathbf{q_1} = (\delta, \delta)$, $\mathbf{q}_2 = (\delta, -2\delta)$, and $\mathbf{q}_3 = (-2\delta, \delta)$, with $\delta = 0.125$. The magnetic unit cell (m.u.c.) of this A2Sk lattice, with a lateral size of approximately 8 crystal lattice constants, encompasses three nanoscale antibiskyrmions; this is why in Fig. 13c the topological charge at low temperatures saturates to a value of 6, each of the three antiskyrmions in the magnetic unit cell having a $|Q| = 2$ topological charge. Each antibiskyrmion has an approximate diameter of 1.6 *nm* and is surrounded by six vortices with a net magnetization of zero. Notably, the spins at the center of the A2Sk have opposite spin components compared to the vortices' centers. In the specific scenario depicted in Fig. 13b, the spins within the antibiskyrmion core and at the vortices' centers point upward and downward, respectively. We conclude this section by not-

ing the formation of the A2Sk lattice to be connected to the SOC-driven symmetric anisotropic exchange, as carefully described in Ref. Amoroso et al. [108].

6.4 Multiferroicity in NiI2: spin-driven ferroelectricity persisting at the monolayer level

In collaboration with the group of Prof. R. Comin and thanks to a joint experiments-theory analysis, we reported for the first time an example of 2D "type II" multiferroic, [113] with MF properties persisting even at the ultimate thickness-limit of a ML. NiI_2 was known to show, in the bulk form, a proper-screw helimagnetic ground state below 59 K, Kurumaji et al. [114] giving rise to electric polarization perpendicular to the helix propagation vector. However, the MF behavior in extremely thin films was unexplored and was therefore addressed by our teams by exfoliating bulk samples and creating "few-layers-thick" samples, characterized both theoretically and experimentally. From the experimental point of view, complementary non-linear optical techniques (optical birefringence and second-harmonic generation, SHG) were used to probe the polar and magnetic orders, as a function of temperature and number of layers, N. The results for NiI_2 few-layer-samples (see Fig. 14a) showed a clear emergence of the non-linear optics signal below a certain ordering temperature, for every number of layers N between one ML and four layers. Therefore, they unambiguously reported the persistence of an ordered phase, down to the ML limit, although with a reducing ordering temperature upon decreasing the thickness. The symmetry-analysis performed on the basis of the optical birefringence results showed, below the ordering temperature, a breaking of the c-axis three-fold rotational symmetry (C_{3z}) and a reduction to a single in-plane two-fold symmetry operation (C_2). These results were consistent with an underlying single-**q** helical magnetic ground state. In addition, using SHG as a probe of inversion symmetry breaking and combining with lowering of rotational symmetry to C_2 previously observed, experiments suggested the presence of a polar order down to the single-layer limit.

From the theoretical point of view, a combined approach based on Monte Carlo and density functional theory simulations was adopted. The presence of anisotropic interactions and exchange frustration, as indicated by DFT, guaranteed the presence of helimagnetic long-range order even in the ML limit. A magneto-electric characterization was also theoretically performed by calculating via DFT the magnetoelectric-coupling tensor **M**, connecting the FE polarization **P** to the cross-product $\mathbf{S}_1 \times \mathbf{S}_2$, via the "generalized" Katsura-Nagaosa-Balatzky (g-KNB [89] model, leading to the expression $\mathbf{P} = \mathbf{M}\,\mathbf{S}_1 \times \mathbf{S}_2$ (as explained in Sect. 4.2). The first-principles estimate led to the following values (in units of 10^{-5} eÅ):

$$\mathbf{M} = \begin{bmatrix} (\mathbf{P}_{12}^{yz})_x & (\mathbf{P}_{12}^{zx})_x & (\mathbf{P}_{12}^{xy})_x \\ (\mathbf{P}_{12}^{yz})_y & (\mathbf{P}_{12}^{zx})_y & (\mathbf{P}_{12}^{xy})_y \\ (\mathbf{P}_{12}^{yz})_z & (\mathbf{P}_{12}^{zx})_z & (\mathbf{P}_{12}^{xy})_z \end{bmatrix} = \begin{bmatrix} 20 & 0 & 32 \\ 0 & 348 & -520 \\ 0 & 25 & 0 \end{bmatrix} \tag{25}$$

The elements of the matrix were found to strongly deviate from those expected in a "standard" KNB model, which would only show one independent non-zero element,

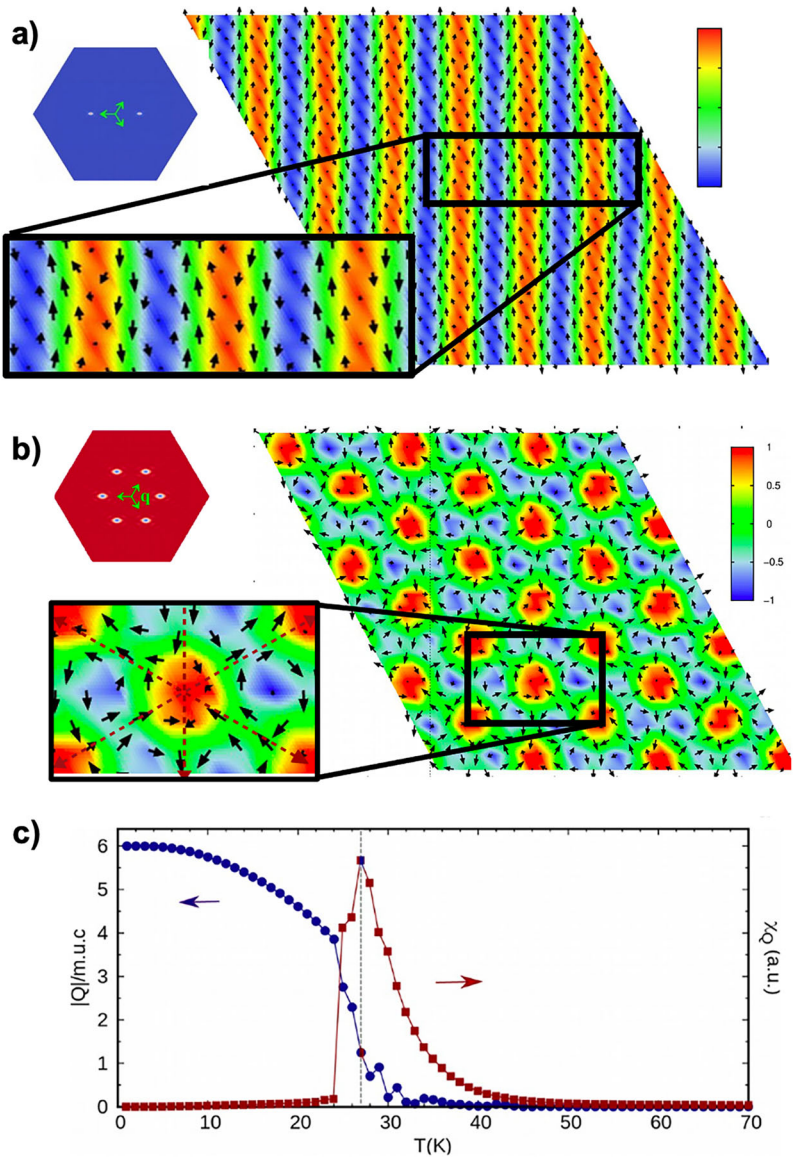

Fig. 13 **a** Snapshot at $T = 1$ K from Monte-Carlo simulations of real-space spin configuration of the spin-helix. The colormap (see right-side color-bar) indicates the out-of-plane S_z spin component. Black arrows denote spin projections on the ML plane. A zoom of the related spin-texture is highlighted by the black rectangle. The associated spin structure factor $\tilde{S}(q)$ is shown by the blue hexagon on the left. **b** Snapshot at $T = 1$ K from Monte-Carlo simulations of real-space spin configuration of the A2Sk lattice. The colormap indicates the out-of-plane S_z spin component. Black arrows denote spin projections on the ML plane. A zoom of the related spin-texture is highlighted by the black rectangle. The associated spin structure factor $\tilde{S}(q)$ is shown by the red hexagon on the left. **c** Topological charge $|Q|$ (blue closed circles) per magnetic unit cell and corresponding topological susceptibility χ_Q (red closed squares) as a function of temperature, pointing to a transition temperature $T_c \sim 28$ K. Figure adapted from Ref. Amoroso et al. [108]

such that $M_{32} = -M_{23}$. When summing over all the Ni spin-couples, arranged on a triangular lattice and assumed to interact via a magnetoelectric-coupling tensor as reported in Eq. 25, we estimated a small polarization to develop in the monolayer plane and to be directed along the spiral propagation vector, at variance with the "standard" KNB model (where **q** and **P** are orthogonal). Moreover, we confirmed polarization to be driven by the magnetic helix (cfr. Fig. 14e), as in every type-II multiferroic, whose direction is fully consistent with that derived from the above-mentioned symmetry analysis of non-linear optics experiments.

7 Conclusions and outlook

We presented an overview of spin–orbit-coupling-related phenomena in solids. Starting from general arguments and recalling atomic-like SOC, we reviewed some of the main effects that SOC gives rise to: (i) in magnetic solids, we discussed magnetic anisotropy and exotic "beyond-Heisenberg" spin–spin interactions (Dzyaloshinskii-Moriya, Kitaev-like, etc), as well as their consequences on some complex spin-textures (skyrmions, spin spirals, etc); (ii) in non-magnetic solids, we presented an overview of peculiar band-splitting effects, such as spin-valley coupling or Rashba-effects (including examples from the class of Ferroelectric Rashba semiconductors); (iii) in multiferroics, we discussed the emergence of ferroelectric polarization as arising from non-collinear spin-textures. In the second part of the review, we analyzed how to estimate SOC-related quantities fully from first-principles (in particular for exchange coupling tensors and magnetoelectric-coupling tensors). Finally, we discussed a few selected examples, where the methodological approaches previously presented were applied to the class of two-dimensional magnetic materials. In closer detail, the first example concerned the first-principles characterization of magnetic properties, focusing in particular on the emergence of a peculiar symmetric anisotropic exchange coupling in Ni-halides. Starting from DFT-derived parameters, we discussed the ground-state spin configuration of NiI_2, which seems to be most intriguing material in the class, as it shows a spin-helix or possibly a topologically non-trivial antiskyrmion lattice. In the last example, we discussed multiferroicity in NiI_2 mono-and few-layers, by presenting a joint theory-experimental work, proposing spin-induced ferroelectricity arising from SOC.

As for the outlook of SOC-related phenomena in the near future, one can anticipate a few directions, as detailed below. While the effects considered in this review are based on a "moderate" coupling between spin and orbital degrees of freedom, part of the scientific community is currently shifting towards the fascinating field of $4d$ and $5d$ based systems (such as iridates, osmates and other complex oxides), where the spin–orbit entanglement becomes predominant. In addition to counteracting the general argument that "SOC effects are weak", $4d$ and $5d$-based materials might be further explored as some complex though exciting quantum phenomena have been proposed or found to emerge, such as multipolar orderings, quantum spin liquids, excitonic magnetism, correlated topological insulators, topological superconductors etc [5, 115]. One can, therefore, easily expect significant progresses in that area; from the theory point of view, this will require not only advances in characteriza-

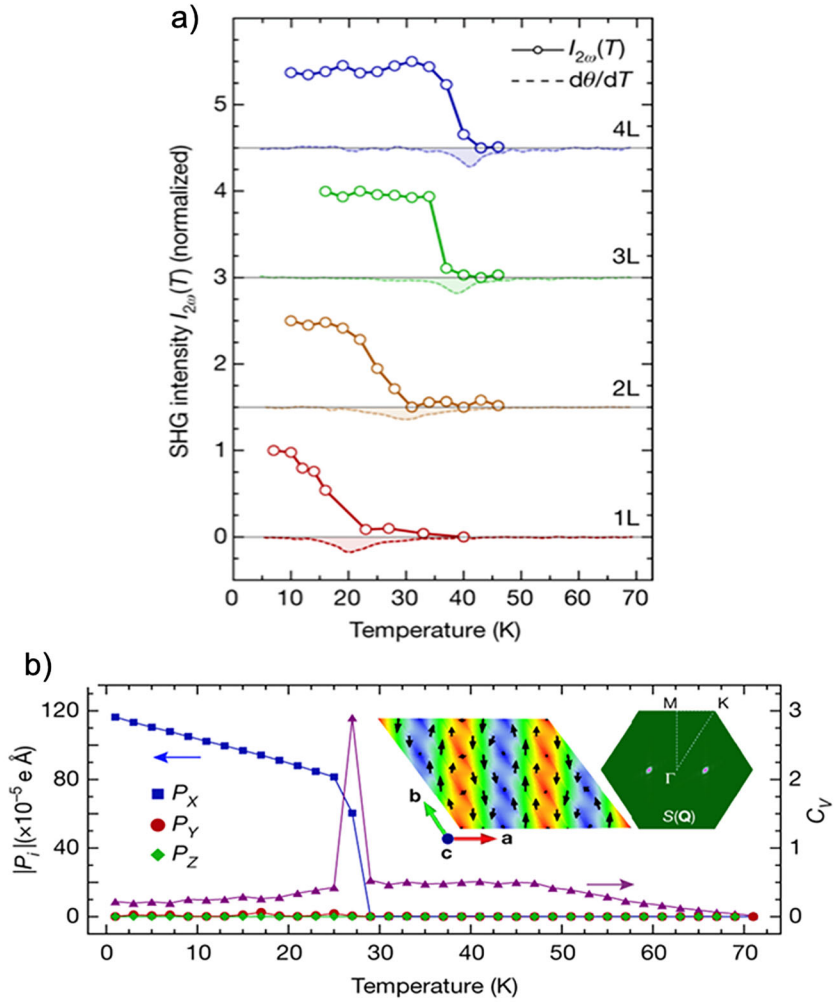

Fig. 14 **a** Electric-dipole-SHG intensity, for one- (1 L) to four-layer (4 L) samples vs temperature T. Dashed curves: temperature-derivative calculated from layer-dependent data. **b** Electric polarization components $|P_i|$ (closed squares) and specific heat (C_V, triangles) vs temperature, relative to the proper-screw spiral order (inset: spin texture, with black arrows and colour map representing in-plane and out-of-plane spin components, respectively: $\tilde{S}(q)$: spin structure factor, corresponding to the single-**q** helical spin configuration. Figure adapted from Ref. Song et al. [113]

tion and in microscopic understanding, but also methodological developments, since the regimes of correlations and spin–orbit entanglement characteristic of 5*d*-based oxides seem to impose going beyond DFT for a realistic modelling, for example by combining DFT with Dynamical Mean Field Theory [116, 117]. Another interesting avenue is the relation between curvature effects and spin–orbit coupling. In closer detail, while flexomagnetism (*i.e.* the study of magnetic properties in the presence of curved geometries) [88] is a fast developing direction in the whole magnetism area,

the connection between SOC and DM interaction, Kitaev exchange, SIA or Rashba-like coupling in cylindrical (or in general curved) geometries is gaining increasing importance [118, 119] and promises interesting outcome in the near future. Last but not least, we mention the booming field of "altermagnetism", Šmejkal et al. [120, 121] its "smoking-gun" being a spin-splitting [122, 123] present in the electronic structure of an antiferromagnet. One of the most interesting features about altermagnetism is that the spin-splitting is not due to SOC and, as such, its energy scale can be much larger than spin–splitting induced by relativistic effects. Still, the coexistence and the interplay between altermagnetism and SOC seems a promising avenue for the near future.

We hope these last examples, along with those previously presented in the review, will further motivate the scientific community towards the exploration of SOC-induced effects, strengthening the role of SOC as an endless source of interesting physics and widening the already rich variety of SOC-driven phenomena.

Acknowledgements I am particularly grateful to Paolo Barone for many enlightening discussions over the years. I would also like to acknowledge all my collaborators, who mostly contributed to the results presented in this review, in particular K. Yamauchi, D. Di Sante, D. Amoroso, S. Stavric, A. Stroppa. The collaboration with R. Comin, R. Bertacco, C. Rinaldi, R. Valenti and their group members is also acknowledged.

Author Contributions SP conceived the entire work and wrote the manuscript.

Funding Open access funding provided by Università degli Studi di Milano - Bicocca within the CRUI-CARE Agreement. This work was supported by the Next-Generation-EU program via the PRIN-2022 SORBET (Grant No. 2022ZY8HJY), the ICSC initiative (National Center for High-Performance Supercomputing, Big Data and Quantum Computing), the PE4 Partenariato Quantum Science and Technology (NQSTI).

Data Availability The datasets generated during and/or analyzed during the current study are available from the corresponding author on reasonable request.

Declarations

Conflict of interest The author has no financial or non-financial interests to disclose.

References

1. J.M.D. Coey, *Magnetism and Magnetic Materials* (Cambridge University Press, Cambridge, 2013)
2. P. Grünberg, R. Schreiber, Y. Pang, M.B. Brodsky, H. Sowers, layered magnetic structures: evidence for antiferromagnetic coupling of Fe layers across Cr interlayers. Phys. Rev. Lett. **57**(19), 2442–2445 (1986). https://doi.org/10.1103/PhysRevLett.57.2442

3. P.A. Grünberg, Nobel lecture: from spin waves to giant magnetoresistance and beyond. Rev. Mod. Phys. **80**(4), 1531–1540 (2008). https://doi.org/10.1103/RevModPhys.80.1531
4. G. Jackeli, G. Khaliullin, Mott insulators in the strong spin-orbit coupling limit: from Heisenberg to a quantum compass and Kitaev models. Phys. Rev. Lett. **102**(1), 017205 (2009). https://doi.org/10.1103/PhysRevLett.102.017205
5. W. Witczak-Krempa, G. Chen, Y.B. Kim, L. Balents, Correlated quantum phenomena in the strong spin-orbit regime. Annu. Rev. Condens. Matter Phys. **5**(1), 57–82 (2014). https://doi.org/10.1146/annurev-conmatphys-020911-125138
6. H.A. Bethe, E.E. Salpeter, Quantum Mechanics of One- and Two-Electron Atoms (Springer. Boston (1977). https://doi.org/10.1007/978-1-4613-4104-8
7. L.H. Thomas, The motion of the spinning electron. Nature **117**(514), 514–514 (1926). https://doi.org/10.1038/117514a0
8. M. Chrysos, The non-intuitive Thomas factor: a heuristic argument with classical electromagnetism. Eur. J. Phys. **27**(1), 1–4 (2006). https://doi.org/10.1088/0143-0807/27/1/001
9. D.I. Khomskii, *Transition Metal Compounds* (Cambridge University Press, Cambridge, 2014). https://doi.org/10.1017/CBO9781139096782
10. S.V. Streltsov, D.I. Khomskii, Orbital physics in transition metal compounds: new trends. Phys. Usp. **60**(11), 1121–1146 (2017). https://doi.org/10.3367/UFNe.2017.08.038196
11. A. Manchon, H.C. Koo, J. Nitta, S.M. Frolov, R.A. Duine, New perspectives for Rashba spin-orbit coupling. Nat. Mater. **14**(9), 871–882 (2015). https://doi.org/10.1038/nmat4360
12. J. Sinova, S.O. Valenzuela, J. Wunderlich, C. Back, T. Jungwirth, Spin hall effects. Rev. Mod. Phys. **87**(4), 1213–1260 (2015). https://doi.org/10.1103/RevModPhys.87.1213
13. M.I. D'Yakonov, V.I. Perel', Possibility of orienting electron spins with current. Sov. J. Exp. Theor. Phys. Lett. **13**, 467 (1971)
14. J.E. Hirsch, Spin hall effect. Phys. Rev. Lett. **83**(9), 1834–1837 (1999). https://doi.org/10.1103/PhysRevLett.83.1834
15. B.A. Bernevig, O. Vafek, Piezo-magnetoelectric effects in *p*-doped semiconductors. Phys. Rev. B **72**(3), 033203 (2005). https://doi.org/10.1103/PhysRevB.72.033203
16. A. Manchon, S. Zhang, Theory of nonequilibrium intrinsic spin torque in a single nanomagnet. Phys. Rev. B **78**(21), 212405 (2008). https://doi.org/10.1103/PhysRevB.78.212405
17. V.M. Edelstein, Spin polarization of conduction electrons induced by electric current in two-dimensional asymmetric electron systems. Solid State Commun. **73**(3), 233–235 (1990). https://doi.org/10.1016/0038-1098(90)90963-C
18. H.J.F. Jansen, Magnetic anisotropy in density-functional theory. Phys. Rev. B **38**(12), 8022–8029 (1988). https://doi.org/10.1103/PhysRevB.38.8022
19. D. Gatteschi, R. Sessoli, J. Villain, *Molecular Nanomagnets, Mesoscopic Physics and Nanotechnology*, vol. 5 (Oxford University Press, Oxford, 2006)
20. I. Dzyaloshinsky, A thermodynamic theory of "weak" ferromagnetism of antiferromagnetics. J. Phys. Chem. Solids **4**(4), 241–255 (1958). https://doi.org/10.1016/0022-3697(58)90076-3
21. T. Moriya, Anisotropic superexchange interaction and weak ferromagnetism. Phys. Rev. **120**(1), 91–98 (1960). https://doi.org/10.1103/PhysRev.120.91
22. A. Kitaev, Anyons in an exactly solved model and beyond. Ann. Phys. **321**, 2–111 (2006)
23. M. Faehnle, H. Kronmueller, Micromagnetic theory of phase transitions in inhomogeneous ferromagnets. II. Appl. Phys. Status Solidi (b) **98**(1), 219–228 (1980). https://doi.org/10.1002/pssb.2220980121
24. T. Moriya, New mechanism of anisotropic superexchange interaction. Phys. Rev. Lett. **4**(5), 228–230 (1960). https://doi.org/10.1103/PhysRevLett.4.228
25. J. Ni, X. Li, D. Amoroso, X. He, J. Feng, E. Kan, S. Picozzi, H. Xiang, Giant biquadratic exchange in 2D magnets and its role in stabilizing ferromagnetism of $NiCl_2$ monolayers. Phys. Rev. Lett. **127**(24), 247204 (2021). https://doi.org/10.1103/PhysRevLett.127.247204
26. S. Paul, S. Haldar, S. Von Malottki, S. Heinze, Role of higher-order exchange interactions for skyrmion stability. Nat. Commun. **11**(1), 4756 (2020). https://doi.org/10.1038/s41467-020-18473-x
27. A.N. Bogdanov, U.K. Rößler, Chiral symmetry breaking in magnetic thin films and multilayers. Phys. Rev. Lett. **87**(3), 037203 (2001). https://doi.org/10.1103/PhysRevLett.87.037203
28. S. Heinze, K. Von Bergmann, M. Menzel, J. Brede, A. Kubetzka, R. Wiesendanger, G. Bihlmayer, S. Blügel, Spontaneous atomic-scale magnetic skyrmion lattice in two dimensions. Nat. Phys. **7**(9), 713–718 (2011). https://doi.org/10.1038/nphys2045

29. N. Nagaosa, Y. Tokura, Topological properties and dynamics of magnetic skyrmions. Nat. Nanotechnol. **8**(12), 899–911 (2013). https://doi.org/10.1038/nnano.2013.243
30. B. Göbel, I. Mertig, O.A. Tretiakov, Beyond skyrmions: review and perspectives of alternative magnetic quasiparticles. Phys. Rep. **895**, 1–28 (2021). https://doi.org/10.1016/j.physrep.2020.10.001
31. Y.A. Bychkov, E.I. Rashba, Oscillatory effects and the magnetic susceptibility of carriers in inversion layers. J. Phys. C: Solid State Phys. **17**(33), 6039–6045 (1984). https://doi.org/10.1088/0022-3719/17/33/015
32. R. Winkler, U. Zülicke, Theory of electric, magnetic, and toroidal polarizations in crystalline solids with applications to hexagonal lonsdaleite and cubic diamond. Phys. Rev. B **107**(15), 155201 (2023). https://doi.org/10.1103/PhysRevB.107.155201
33. G. Bihlmayer, O. Rader, R. Winkler, Focus on the rashba effect. New J. Phys. **17**(5), 050202 (2015). https://doi.org/10.1088/1367-2630/17/5/050202
34. G. Dresselhaus, Spin-orbit coupling effects in zinc blende structures. Phys. Rev. **100**(2), 580–586 (1955). https://doi.org/10.1103/PhysRev.100.580
35. K. Ishizaka, M.S. Bahramy, H. Murakawa, M. Sakano, T. Shimojima, T. Sonobe, K. Koizumi, S. Shin, H. Miyahara, A. Kimura, K. Miyamoto, T. Okuda, H. Namatame, M. Taniguchi, R. Arita, N. Nagaosa, K. Kobayashi, Y. Murakami, R. Kumai, Y. Kaneko, Y. Onose, Y. Tokura, Giant Rashba-type spin splitting in bulk BiTeI. Nat. Mater. **10**(7), 521–526 (2011). https://doi.org/10.1038/nmat3051
36. X. Zhang, Q. Liu, J.-W. Luo, A.J. Freeman, A. Zunger, Hidden spin polarization in inversion-symmetric bulk crystals. Nat. Phys. **10**(5), 387–393 (2014). https://doi.org/10.1038/nphys2933
37. K.M. Rabe (ed.), *Physics of Ferroelectrics: A Modern Perspective, Topics in Applied Physics*, vol. 105 (Springer, Berlin, 2007)
38. D. Di Sante, P. Barone, R. Bertacco, S. Picozzi, Electric control of the giant Rashba effect in bulk GeTe. Adv. Mater. **25**(4), 509–513 (2013). https://doi.org/10.1002/adma.201203199
39. S. Picozzi, Ferroelectric Rashba semiconductors as a novel class of multifunctional materials. Front. Phys. **2**(10), 1 (2014). https://doi.org/10.3389/fphy.2014.00010
40. M. Liebmann, C. Rinaldi, D. Di Sante, J. Kellner, C. Pauly, R.N. Wang, J.E. Boschker, A. Giussani, S. Bertoli, M. Cantoni, L. Baldrati, M. Asa, I. Vobornik, G. Panaccione, D. Marchenko, J. Sánchez-Barriga, O. Rader, R. Calarco, S. Picozzi, R. Bertacco, M. Morgenstern, Giant Rashba-type spin splitting in ferroelectric GeTe (111). Adv. Mater. **28**(3), 560–565 (2016). https://doi.org/10.1002/adma.201503459
41. S. Varotto, L. Nessi, S. Cecchi, J. Sławińska, P. Noël, S. Petrò, F. Fagiani, A. Novati, M. Cantoni, D. Petti, E. Albisetti, M. Costa, R. Calarco, M. Buongiorno Nardelli, M. Bibes, S. Picozzi, J.-P. Attané, L. Vila, R. Bertacco, C. Rinaldi, Room-temperature ferroelectric switching of spin-to-charge conversion in germanium telluride. Nat. Electron. **4**(10), 740–747 (2021). https://doi.org/10.1038/s41928-021-00653-2
42. D. Pesin, A.H. MacDonald, Spintronics and pseudospintronics in graphene and topological insulators. Nat. Mater. **11**(5), 409–416 (2012). https://doi.org/10.1038/nmat3305
43. X.-J. Liu, M.F. Borunda, X. Liu, J. Sinova, Effect of induced spin-orbit coupling for atoms via laser fields. Phys. Rev. Lett. **102**(4), 046402 (2009). https://doi.org/10.1103/PhysRevLett.102.046402
44. X. Xu, W. Yao, D. Xiao, T.F. Heinz, Spin and pseudospins in layered transition metal dichalcogenides. Nat. Phys. **10**(5), 343–350 (2014). https://doi.org/10.1038/nphys2942
45. X.-L. Qi, S.-C. Zhang, Topological insulators and superconductors. Rev. Mod. Phys. **83**(4), 1057–1110 (2011). https://doi.org/10.1103/RevModPhys.83.1057
46. B.J. Wieder, B. Bradlyn, J. Cano, Z. Wang, M.G. Vergniory, L. Elcoro, A.A. Soluyanov, C. Felser, T. Neupert, N. Regnault, B.A. Bernevig, Topological materials discovery from crystal symmetry. Nat. Rev. Mater. **7**(3), 196–216 (2021). https://doi.org/10.1038/s41578-021-00380-2
47. B.A. Bernevig, C. Felser, H. Beidenkopf, Progress and prospects in magnetic topological materials. Nature **603**(7899), 41–51 (2022). https://doi.org/10.1038/s41586-021-04105-x
48. M.Z. Hasan, G. Chang, I. Belopolski, G. Bian, S.-Y. Xu, J.-X. Yin, Weyl, Dirac and high-fold chiral fermions in topological quantum matter. Nat. Rev. Mater. **6**(9), 784–803 (2021). https://doi.org/10.1038/s41578-021-00301-3
49. J.-X. Yin, B. Lian, M.Z. Hasan, Topological kagome magnets and superconductors. Nature **612**(7941), 647–657 (2022). https://doi.org/10.1038/s41586-022-05516-0
50. D.J. Thouless, M. Kohmoto, M.P. Nightingale, M. Den Nijs, Quantized Hall conductance in a two-dimensional periodic potential. Phys. Rev. Lett. **49**(6), 405–408 (1982). https://doi.org/10.1103/PhysRevLett.49.405

51. M. König, S. Wiedmann, C. Brüne, A. Roth, H. Buhmann, L.W. Molenkamp, X.-L. Qi, S.-C. Zhang, Quantum spin Hall insulator state in HgTe quantum wells. Science **318**(5851), 766–770 (2007). https://doi.org/10.1126/science.1148047
52. X.-L. Qi, S.-C. Zhang, The quantum spin Hall effect and topological insulators. Phys. Today **63**(1), 33–38 (2010). https://doi.org/10.1063/1.3293411
53. H. Zhang, C.-X. Liu, X.-L. Qi, X. Dai, Z. Fang, S.-C. Zhang, Topological insulators in Bi_2Se_3, Bi_2Te_3 and Sb_2Te_3 with a single Dirac cone on the surface. Nat. Phys. **5**(6), 438–442 (2009). https://doi.org/10.1038/nphys1270
54. D. Hsieh, Y. Xia, L. Wray, D. Qian, A. Pal, J.H. Dil, J. Osterwalder, F. Meier, G. Bihlmayer, C.L. Kane, Y.S. Hor, R.J. Cava, M.Z. Hasan, Observation of unconventional quantum spin textures in topological insulators. Science **323**(5916), 919–922 (2009). https://doi.org/10.1126/science.1167733
55. K.L. Wang, Y. Wu, C. Eckberg, G. Yin, Q. Pan, Topological quantum materials. MRS Bull. **45**(5), 373–379 (2020). https://doi.org/10.1557/mrs.2020.122
56. J. Wang, J.B. Neaton, H. Zheng, V. Nagarajan, S.B. Ogale, B. Liu, D. Viehland, V. Vaithyanathan, D.G. Schlom, U.V. Waghmare, N.A. Spaldin, K.M. Rabe, M. Wuttig, R. Ramesh, Epitaxial $BiFeO_3$ multiferroic thin film heterostructures. Science **299**(5613), 1719–1722 (2003). https://doi.org/10.1126/science.1080615
57. N.A. Spaldin, R. Ramesh, Advances in magnetoelectric multiferroics. Nat. Mater. **18**(3), 203–212 (2019). https://doi.org/10.1038/s41563-018-0275-2
58. M. Bibes, A. Barthélémy, Towards a magnetoelectric memory. Nat. Mater. **7**(6), 425–426 (2008). https://doi.org/10.1038/nmat2189
59. M. Fiebig, T. Lottermoser, D. Meier, M. Trassin, The evolution of multiferroics. Nat. Rev. Mater. **1**(8), 16046 (2016). https://doi.org/10.1038/natrevmats.2016.46
60. D. Khomskii, Classifying multiferroics: mechanisms and effects. Physics **2**, 20 (2009). https://doi.org/10.1103/Physics.2.20
61. T. Kimura, T. Goto, H. Shintani, K. Ishizaka, T. Arima, Y. Tokura, Magnetic control of ferroelectric polarization. Nature **426**(6962), 55–58 (2003). https://doi.org/10.1038/nature02018
62. S. Dong, H. Xiang, E. Dagotto, Magnetoelectricity in multiferroics: a theoretical perspective. Natl. Sci. Rev. **6**(4), 629–641 (2019). https://doi.org/10.1093/nsr/nwz023
63. I.A. Sergienko, E. Dagotto, Role of the Dzyaloshinskii-Moriya interaction in multiferroic perovskites. Phys. Rev. B **73**(9), 094434 (2006). https://doi.org/10.1103/PhysRevB.73.094434
64. H. Katsura, N. Nagaosa, A.V. Balatsky, Spin current and magnetoelectric effect in noncollinear magnets. Phys. Rev. Lett. **95**(5), 057205 (2005). https://doi.org/10.1103/PhysRevLett.95.057205
65. M. Mostovoy, Ferroelectricity in spiral magnets. Phys. Rev. Lett. **96**(6), 067601 (2006). https://doi.org/10.1103/PhysRevLett.96.067601
66. C. Lacroix, P. Mendels, F. Mila (eds.), *Introduction to Frustrated Magnetism: Materials, Experiments, Theory, 1*, Springer Series in Solid-State Sciences, vol. 164, 2011th edn. (Springer, Berlin, 2013)
67. B. Normand, Frontiers in frustrated magnetism. Contemp. Phys. **50**(4), 533–552 (2009). https://doi.org/10.1080/00107510902850361
68. R.D. King-Smith, D. Vanderbilt, Theory of polarization of crystalline solids. Phys. Rev. B **47**(3), 1651–1654 (1993). https://doi.org/10.1103/PhysRevB.47.1651
69. R. Resta, Macroscopic polarization in crystalline dielectrics: the geometric phase approach. Rev. Mod. Phys. **66**(3), 899–915 (1994). https://doi.org/10.1103/RevModPhys.66.899
70. P. Hohenberg, W. Kohn, Inhomogeneous electron gas. Phys. Rev. **136**(3B), 864–871 (1964). https://doi.org/10.1103/PhysRev.136.B864
71. W. Kohn, L.J. Sham, Self-consistent equations including exchange and correlation effects. Phys. Rev. **140**(4A), 1133–1138 (1965). https://doi.org/10.1103/PhysRev.140.A1133
72. V.I. Anisimov, A.I. Poteryaev, M.A. Korotin, A.O. Anokhin, G. Kotliar, First-principles calculations of the electronic structure and spectra of strongly correlated systems: dynamical mean-field theory. J. Phys.: Condens. Matter **9**(35), 7359–7367 (1997). https://doi.org/10.1088/0953-8984/9/35/010
73. S. Steiner, S. Khmelevskyi, M. Marsmann, G. Kresse, Calculation of the magnetic anisotropy with projected-augmented-wave methodology and the case study of disordered Fe_{1-x} Co_x alloys. Phys. Rev. B **93**(22), 224425 (2016). https://doi.org/10.1103/PhysRevB.93.224425
74. G. Kresse, J. Hafner, Ab initio molecular dynamics for liquid metals. Phys. Rev. B **47**(1), 558–561 (1993). https://doi.org/10.1103/PhysRevB.47.558

75. G. Kresse, J. Furthmüller, Efficient iterative schemes for ab initio total-energy calculations using a plane-wave basis set. Phys. Rev. B **54**(16), 11169–11186 (1996). https://doi.org/10.1103/PhysRevB.54.11169
76. G. Kresse, J. Furthmüller, Efficiency of ab-initio total energy calculations for metals and semiconductors using a plane-wave basis set. Comput. Mater. Sci. **6**(1), 15–50 (1996). https://doi.org/10.1016/0927-0256(96)00008-0
77. P.E. Blöchl, Projector augmented-wave method. Phys. Rev. B **50**(24), 17953–17979 (1994). https://doi.org/10.1103/PhysRevB.50.17953
78. L. Belpassi, M. De Santis, H.M. Quiney, F. Tarantelli, L. Storchi, BERTHA: Implementation of a four-component Dirac-Kohn-Sham relativistic framework. J. Chem. Phys. **152**(16), 164118 (2020). https://doi.org/10.1063/5.0002831
79. A.I. Liechtenstein, M.I. Katsnelson, V.P. Antropov, V.A. Gubanov, Local spin density functional approach to the theory of exchange interactions in ferromagnetic metals and alloys. J. Magn. Magn. Mater. **67**(1), 65–74 (1987). https://doi.org/10.1016/0304-8853(87)90721-9
80. M.I. Katsnelson, A.I. Lichtenstein, First-principles calculations of magnetic interactions in correlated systems. Phys. Rev. B **61**(13), 8906–8912 (2000). https://doi.org/10.1103/PhysRevB.61.8906
81. S. Lounis, P.H. Dederichs, Mapping the magnetic exchange interactions from first principles: anisotropy anomaly and application to Fe, Ni, and Co. Phys. Rev. B **82**(18), 180404 (2010). https://doi.org/10.1103/PhysRevB.82.180404
82. F. Illas, I.P.R. Moreira, C. De Graaf, V. Barone, Magnetic coupling in biradicals, binuclear complexes and wide-gap insulators: a survey of ab initio wave function and density functional theory approaches. Theor. Chem. Acc. Theory Comput. Model. Theor. Chim. Acta **104**(3—-4), 265–272 (2000). https://doi.org/10.1007/s002140000133
83. J.P. Malrieu, R. Caballol, C.J. Calzado, C. De Graaf, N. Guihéry, Magnetic interactions in molecules and highly correlated materials: physical content, analytical derivation, and rigorous extraction of magnetic Hamiltonians. Chem. Rev. **114**(1), 429–492 (2014). https://doi.org/10.1021/cr300500z
84. H. Xiang, C. Lee, H.-J. Koo, X. Gong, M.-H. Whangbo, Magnetic properties and energy-mapping analysis. Dalton Trans. **42**(4), 823–853 (2013). https://doi.org/10.1039/C2DT31662E
85. X. Li, H. Yu, F. Lou, J. Feng, M.-H. Whangbo, H. Xiang, Spin Hamiltonians in magnets: theories and computations. Molecules **26**(4), 803 (2021). https://doi.org/10.3390/molecules26040803
86. C. Xu, H. Yu, J. Wang, H. Xiang, First-principles approaches to magnetoelectric multiferroics. Annu. Rev. Condens. Matter Phys. **15**(1), 85–108 (2024). https://doi.org/10.1146/annurev-conmatphys-032922-102353
87. C. Bigi, L. Qiao, C. Liu, P. Barone, M.C. Hatnean, G.-R. Siemann, B. Achinuq, D.A. Mayoh, G. Vinai, V. Polewczyk, D. Dagur, F. Mazzola, P. Bencok, T. Hesjedal, G. Van Der Laan, W. Ren, G. Balakrishnan, S. Picozzi, P.D.C. King, Covalency, correlations, and interlayer interactions governing the magnetic and electronic structure of $Mn_3Si_2Te_6$. Phys. Rev. B **108**(5), 054419 (2023). https://doi.org/10.1103/PhysRevB.108.054419
88. D. Makarov, O.M. Volkov, A. Kákay, O.V. Pylypovskyi, B. Budinská, O.V. Dobrovolskiy, New dimension in magnetism and superconductivity: 3D and curvilinear nanoarchitectures. Adv. Mater. **34**(3), 2101758 (2022). https://doi.org/10.1002/adma.202101758
89. H.J. Xiang, E.J. Kan, Y. Zhang, M.-H. Whangbo, X.G. Gong, General theory for the ferroelectric polarization induced by spin-spiral order. Phys. Rev. Lett. **107**(15), 157202 (2011). https://doi.org/10.1103/PhysRevLett.107.157202
90. M. Fiebig, Revival of the magnetoelectric effect. J. Phys. D Appl. Phys. **38**(8), 123–152 (2005). https://doi.org/10.1088/0022-3727/38/8/R01
91. J. Íñiguez, First-principles approach to lattice-mediated magnetoelectric effects. Phys. Rev. Lett. **101**(11), 117201 (2008). https://doi.org/10.1103/PhysRevLett.101.117201
92. K.S. Novoselov, A.K. Geim, S.V. Morozov, D. Jiang, Y. Zhang, S.V. Dubonos, I.V. Grigorieva, A.A. Firsov, Electric field effect in atomically thin carbon films. Science **306**(5696), 666–669 (2004). https://doi.org/10.1126/science.1102896
93. J.-U. Lee, S. Lee, J.H. Ryoo, S. Kang, T.Y. Kim, P. Kim, C.-H. Park, J.-G. Park, H. Cheong, Ising-type magnetic ordering in atomically thin $FePS_3$. Nano Lett. **16**(12), 7433–7438 (2016). https://doi.org/10.1021/acs.nanolett.6b03052
94. C. Gong, L. Li, Z. Li, H. Ji, A. Stern, Y. Xia, T. Cao, W. Bao, C. Wang, Y. Wang, Z.Q. Qiu, R.J. Cava, S.G. Louie, J. Xia, X. Zhang, Discovery of intrinsic ferromagnetism in two-dimensional van der Waals crystals. Nature **546**(7657), 265–269 (2017). https://doi.org/10.1038/nature22060

95. B. Huang, G. Clark, E. Navarro-Moratalla, D.R. Klein, R. Cheng, K.L. Seyler, D. Zhong, E. Schmidgall, M.A. McGuire, D.H. Cobden, W. Yao, D. Xiao, P. Jarillo-Herrero, X. Xu, Layer-dependent ferromagnetism in a van der Waals crystal down to the monolayer limit. Nature **546**(7657), 270–273 (2017). https://doi.org/10.1038/nature22391
96. D.L. Cortie, G.L. Causer, K.C. Rule, H. Fritzsche, W. Kreuzpaintner, F. Klose, Two-dimensional magnets: forgotten history and recent progress towards spintronic applications. Adv. Funct. Mater. **30**(18), 1901414 (2020). https://doi.org/10.1002/adfm.201901414
97. L. Onsager, Crystal statistics. I. A two-dimensional model with an order–disorder transition. Phys. Rev. **65**(3–4), 117–149 (1944). https://doi.org/10.1103/PhysRev.65.117
98. R. Plumier, Neutron diffraction study of magnetic stacking faults in antiferromagnetic K_2NiF_4. J. Appl. Phys. **35**(3), 950–951 (1964). https://doi.org/10.1063/1.1713554
99. M. Hase, I. Terasaki, K. Uchinokura, Observation of the spin-Peierls transition in linear Cu^{2+} (spin-1/2) chains in an inorganic compound $CuGeO_3$. Phys. Rev. Lett. **70**(23), 3651–3654 (1993). https://doi.org/10.1103/PhysRevLett.70.3651
100. N.D. Mermin, H. Wagner, Absence of ferromagnetism or antiferromagnetism in one- or two-dimensional isotropic Heisenberg models. Phys. Rev. Lett. **17**(22), 1133–1136 (1966). https://doi.org/10.1103/PhysRevLett.17.1133
101. R. Miranda, F. Ynduráin, D. Chandesris, J. Lecante, Y. Petroff, Magnetic exchange splitting of one layer of cobalt deposited on top of the (111) surface of copper. Phys. Rev. B **25**(1), 527–530 (1982). https://doi.org/10.1103/PhysRevB.25.527
102. J. Kohlhepp, H.J. Elmers, S. Cordes, U. Gradmann, Power laws of magnetization in ferromagnetic monolayers and the two-dimensional Ising model. Phys. Rev. B **45**(21), 12287–12291 (1992). https://doi.org/10.1103/PhysRevB.45.12287
103. X. Jiang, Q. Liu, J. Xing, N. Liu, Y. Guo, Z. Liu, J. Zhao, Recent progress on 2D magnets: fundamental mechanism, structural design and modification. Appl. Phys. Rev. **8**(3), 031305 (2021). https://doi.org/10.1063/5.0039979
104. M. Gibertini, M. Koperski, A.F. Morpurgo, K.S. Novoselov, Magnetic 2D materials and heterostructures. Nat. Nanotechnol. **14**(5), 408–419 (2019). https://doi.org/10.1038/s41565-019-0438-6
105. M. McGuire, Crystal and magnetic structures in layered, transition metal dihalides and trihalides. Curr. Comput. Aided Drug Des. **7**(5), 121 (2017). https://doi.org/10.3390/cryst7050121
106. B. Huang, M.A. McGuire, A.F. May, D. Xiao, P. Jarillo-Herrero, X. Xu, Emergent phenomena and proximity effects in two-dimensional magnets and heterostructures. Nat. Mater. **19**(12), 1276–1289 (2020). https://doi.org/10.1038/s41563-020-0791-8
107. K. Riedl, D. Amoroso, S. Backes, A. Razpopov, T.P.T. Nguyen, K. Yamauchi, P. Barone, S.M. Winter, S. Picozzi, R. Valentí, Microscopic origin of magnetism in monolayer 3D transition metal dihalides. Phys. Rev. B **106**(3), 035156 (2022). https://doi.org/10.1103/PhysRevB.106.035156
108. D. Amoroso, P. Barone, S. Picozzi, Spontaneous skyrmionic lattice from anisotropic symmetric exchange in a Ni-halide monolayer. Nat. Commun. **11**(1), 5784 (2020). https://doi.org/10.1038/s41467-020-19535-w
109. B. Berg, M. Lüscher, Definition and statistical distributions of a topological number in the lattice O(3) σ-model. Nucl. Phys. B **190**(2), 412–424 (1981). https://doi.org/10.1016/0550-3213(81)90568-X
110. F. Aryasetiawan, M. Imada, A. Georges, G. Kotliar, S. Biermann, A.I. Lichtenstein, Frequency-dependent local interactions and low-energy effective models from electronic structure calculations. Phys. Rev. B **70**(19), 195104 (2004). https://doi.org/10.1103/PhysRevB.70.195104
111. P.W. Anderson, Antiferromagnetism. Theory of superexchange interaction. Phys. Rev. **79**(2), 350–356 (1950). https://doi.org/10.1103/PhysRev.79.350
112. J. Kanamori, Superexchange interaction and symmetry properties of electron orbitals. J. Phys. Chem. Solids **10**(2–3), 87–98 (1959). https://doi.org/10.1016/0022-3697(59)90061-7
113. Q. Song, C.A. Occhialini, E. Ergeçen, B. Ilyas, D. Amoroso, P. Barone, J. Kapeghian, K. Watanabe, T. Taniguchi, A.S. Botana, S. Picozzi, N. Gedik, R. Comin, Evidence for a single-layer van der Waals multiferroic. Nature **602**(7898), 601–605 (2022). https://doi.org/10.1038/s41586-021-04337-x
114. T. Kurumaji, S. Seki, S. Ishiwata, H. Murakawa, Y. Kaneko, Y. Tokura, Magnetoelectric responses induced by domain rearrangement and spin structural change in triangular-lattice helimagnets NiI_2 and CoI_2. Phys. Rev. B **87**(1), 014429 (2013). https://doi.org/10.1103/PhysRevB.87.014429
115. T. Takayama, J. Chaloupka, A. Smerald, G. Khaliullin, H. Takagi, Spin-orbit-entangled electronic phases in 4d and 5d transition-metal compounds. J. Phys. Soc. Jpn. **90**(6), 062001 (2021). https://doi.org/10.7566/JPSJ.90.062001

116. W. Metzner, D. Vollhardt, Correlated lattice fermions in $d = \infty$ dimensions. Phys. Rev. Lett. **62**(9), 1066–1066 (1989). https://doi.org/10.1103/PhysRevLett.62.1066.2
117. A. Georges, G. Kotliar, Hubbard model in infinite dimensions. Phys. Rev. B **45**(12), 6479–6483 (1992). https://doi.org/10.1103/PhysRevB.45.6479
118. A. Edström, D. Amoroso, S. Picozzi, P. Barone, M. Stengel, Curved magnetism in CrI_3. Phys. Rev. Lett. **128**(17), 177202 (2022). https://doi.org/10.1103/PhysRevLett.128.177202
119. P. Gentile, M. Cuoco, C. Ortix, Curvature-induced Rashba spin-orbit interaction in strain-driven nanostructures. SPIN **03**(03), 1340002 (2013). https://doi.org/10.1142/S201032471340002X
120. L. Šmejkal, J. Sinova, T. Jungwirth, Beyond conventional ferromagnetism and antiferromagnetism: a phase with nonrelativistic spin and crystal rotation symmetry. Phys. Rev. X **12**(3), 031042 (2022). https://doi.org/10.1103/PhysRevX.12.031042
121. L. Šmejkal, J. Sinova, T. Jungwirth, Emerging research landscape of altermagnetism. Phys. Rev. X **12**(4), 040501 (2022). https://doi.org/10.1103/PhysRevX.12.040501
122. L.-D. Yuan, Z. Wang, J.-W. Luo, E.I. Rashba, A. Zunger, Giant momentum-dependent spin splitting in centrosymmetric low-Z antiferromagnets. Phys. Rev. B **102**(1), 014422 (2020). https://doi.org/10.1103/PhysRevB.102.014422
123. L. Yuan, A. Zunger, Degeneracy removal of spin bands in collinear antiferromagnets with non-interconvertible spin-structure motif pair. Adv. Mater. **35**(31), 2211966 (2023). https://doi.org/10.1002/adma.202211966